

Physics informed neural network for forward and inverse radiation heat transfer in graded-index medium.

K. Murari * S. Sundar *

December 25, 2024

*Centre for Computational Mathematics and Data Science
Department of Mathematics, IIT Madras, Chennai 600036, India
kmurari2712@gmail.com, slnt@iitm.ac.in

Abstract

Radiation heat transfer in a graded-index medium often suffers accuracy problems due to the gradual changes in the refractive index. The finite element method, meshfree, and other numerical methods often struggle to maintain accuracy when applied to this medium. To address this issue, we apply physics-informed neural networks (PINNs)-based machine learning algorithms to simulate forward and inverse problems for this medium. We also provide the theoretical upper bounds. This theoretical framework is validated through numerical experiments of predefined and newly developed models that demonstrate the accuracy and robustness of the algorithms in solving radiation transport problems in the medium. The simulations show that the novel algorithm goes on with numerical stability and effectively mitigates oscillatory errors, even in cases with more pronounced variations in the refractive index.

Keywords: Radiation transfer, Graded-index, Forward Problems, Inverse Problems, Total Error.

1 Introduction

Radiation heat transfer in graded index materials involves the transmission of thermal energy through electromagnetic waves within a material exhibiting varying refractive index. Typically, this index changes gradually from the center to the material's surface, impacting radiation propagation and heat transfer mechanisms. Understanding the complexities of heat transfer in the materials is paramount. Unlike homogeneous materials, which maintain a constant refractive index, graded index materials undergo gradual changes, significantly affecting thermal radiation propagation. The pivotal role of radiation across various applications justifies this focus, ranging from interpreting spectroscopic emissions in celestial bodies [16], nuclear engineering [23], biological tissues [36], thermal insulation [3], gas turbines [38], combustion systems [12] and radiotherapy dose simulation [34]. Numerous researchers have focused on analyzing radiation heat transmission in such media. Various numerical methods, including the Monte Carlo Method [44], Least-Squares Finite Element Method (LSFEM) [26], Discontinuous Finite Element Method (DFEM) [14], Finite Volume Method (FVM) [24], Petrov-Galerkin Method (MLPG) [25], Least-Squares Spectral Element Method (LSSEM) [49], and Spectral Element Method (SEM) [42], have been employed to simulate radiation transport in these complex systems. However, traditional methods like LSFEM, the Galerkin Finite Element Method (GFEM) [49], and specific mesh-free methods [50] suffer from various deficiencies. These methods often exhibit noticeable high-frequency errors or unwanted fluctuations, despite generally providing results that are close to the true solution. Additionally, the Lattice Boltzmann Method (LBM) [27], [46], and Multi-Relaxation Time (MRT) Lattice Boltzmann Method [15], have been applied, but challenges persist in achieving robust solutions.

In recent years, deep learning is an alternative way to avoid the curse of dimensionality. Due to this reason, deep learning has recently been an essential tool in modern technology and advanced research in the last few years. This learning contains many layers of transformations and scalar nonlinearities. Deep learning techniques demonstrate strong capabilities in approximating highly nonlinear functions. Their computational framework, which employs statistical learning and large-scale optimization methods in conjunction with contemporary hardware and software, enhances their capacity to address nonlinear and high-dimensional partial differential equations (PDEs).

Nomenclature

c_o	speed of light	σ	activation function
n	refractive index	T	temperature distribution [K]
s	position vector	$\mathbf{1}_{[\cdot]}$	unit step function
k_e	extinction coefficient	ρ	diffuse reflectivity
Ω	direction vector	$\varepsilon_{\bar{\omega}}$	emissivity
Φ	scattering phase function	Θ	dimensionless temperature
k_a	absorption coefficient	L	length
k_s	scattering coefficient	μ	directional cosine
T_g	medium temperature [K]	ρ_m	saterial density
Ω'	incoming direction	σ_B	Stefan-Boltzmann constant
\hat{n}_{ω}	normal vector to surface	I_c	collimated intensity from laser
Ω_{rs}	incident direction of specular reflection	I_d	diffuse intensity
I_{bw}	black body intensity	ω	scattering albedo
I	radiative intensity	b	black-body state
S	source term of differential equation	$0, L$	left and right boundaries
$G(s, t)$	incident radiation	$\mathbf{i}, \mathbf{j}, \mathbf{k}$	unit vectors
$q(s, t)$	heat flux [W m^{-2}]	λ	learning rate
ρ^{spce}	specular reflectivity	λ_{reg}	regularization parameters
$K - 1$	number of hidden layers	Ω	outgoing direction
n_{θ}	number of times model retrained in parallel	\tanh	hyperbolic tangent(activation function)
N_{int}	number of interior points	N_{sb}	number of Sobol points
N_{tb}	number of temporal points	N_d	number of data points
N	number of collocations or training points		

Deep neural networks (DNNs) are well known for their ability to universally approximate functions, a property that holds under certain conditions, as demonstrated by Cybenko [7], Hornik et al. [18], Barron [4], and Yarotsky [45]. This property makes them suitable as trial functions for solving PDEs, often by minimizing the residual of the PDE at selected collocation points within the domain. The application of deep learning using DNNs has revolutionized numerous domains, including image and text categorization, machine vision, computational linguistics, voice recognition, self-governing systems, robotics, artificial intelligence in gaming, medical analysis, pharmaceutical research, climate simulation, financial prediction, and protein structure determination. These advancements highlight the versatility and effectiveness of DNNs in tackling complex problems across diverse domains. A technique involves utilizing DNNs founded on explicit or partially explicit representation formulas applicable to parabolic and elliptic partial differential equations (PDEs). Researchers leverage this compositional structure to enhance the approximation capabilities of DNNs. Researchers such as [18], [13], and [5], among others, have introduced and examined this technique for a range of parametric elliptic and parabolic PDEs. In [22], authors discussed a similar approach for approximating linear transport equations with DNNs. A key deep learning algorithm, Physics-Informed Neural Networks (PINNs) [35] is a mesh-free method. PINNs has been successfully applied in supervised, semi-supervised, and unsupervised learning frameworks. PINNs provide solutions for both forward and inverse modeling problems within a unified optimization framework. This algorithm is remarkably adaptable to both continuous and discrete forms of PDEs. For continuous time modeling, PINNs approximate solutions by estimating spatio-temporal functions. For discrete time modeling, PINNs utilize implicit Runge-Kutta time-stepping techniques, allowing for an arbitrary number of time steps. This flexibility has led to the development of extensions such as XPINN [20], cPINN [21], Parallel PINN [39], and Gradient-Enhanced PINN [48]. In addition, the Deepxde library [28] facilitates solving PDEs using PINNs. Recent studies, such as those by Dolean et al. [11] and Moseley et al. [32], have applied domain decomposition approaches to modify PINN, and theoretical error bounds for XPINN have been established for the Navier-Stokes equations [9] and Kolmogorov PDEs [8]. However, there is still limited understanding of why these models occasionally fail to train effectively. Wang et al. [43] explore this issue through the framework of the neural tangent kernel. A recent study by Mishra and Molinaro examines the generalization error of addressing forward problems [31] and inverse problems [30] across various linear and nonlinear partial differential equations (PDEs). The authors have also estimated generalized error bounds for the problems. The authors also worked on nonlinear dispersive PDEs [2], where they derived generalized error bounds for forward problems. The study investigates the stability characteristics of the underlying PDE, utilizing these features to assess generalization errors in connection with training errors. Furthermore, [10] introduces an innovative modification of PINNs called weak PINNs (wPINNs).

PINNs have been used to simulate both forward and inverse problems in the context of radiation transport. Mishra et al. [29] developed a PINN-based algorithm for simulating radiation transport, establishing generalized error bounds for forward problems. Other studies, such as those by Huhn et al. [19] and Riganti et al. [37], have further applied PINNs to solve radiation transport problems in various configurations. The present work simulates both new and existing models for radiation heat transfer in graded-index media. We employ unsupervised PINN algorithms to simulate both predefined and newly developed models, demonstrating improved performance over traditional methods such as finite element methods (e.g., GFEM, LSFEM, DFEM), mesh-free methods, and MRT lattice Boltzmann methods. The results show that our PINN-based approach mitigates the challenges of oscillatory errors and achieves stable, accurate results even with complex variations in the refractive index.

The paper is structured as follows: Section 2 outlines the mathematical model and methodology, including the problem statement, PINN approximation, and key components such as the model, domain, quadrature rules, neural networks, residuals, loss functions, and optimization. Section 3 presents numerical simulations and accuracy verification of the proposed method, while Section 4 discusses the conclusion. An appendix is provided to estimate generalization errors and analyze the impact of optical parameters on radiometric quantities.

2 Problem statement and PINN approximation

Precise prediction of radiative transfer in these circumstances relies on resolving the Radiative Transfer Equation (RTE), an intricate integro-differential equation encompassing seven variables: three spatial coordinates, polar and azimuthal angles, time, and spectral dimensions. The complexity increases in graded-index media, where the curved radiation path, described by the Fermat principle, introduces an additional layer of intricacy, rendering analytical solutions unattainable except in specific limiting cases. Therefore, developing accurate, simple, and efficient tools to solve the RTE in these scenarios becomes imperative for advancing understanding and practical applications. Traditional methods, such as mesh-free or finite-element approaches, struggle with these complexities due to the difficulty of accurately capturing the light's curved path in graded-index media, which often leads to numerical instability and high computational cost. Snell's Law and the Fermat principle [25] are closely related concepts that describe different aspects of light propagation but are fundamentally connected. Snell's Law [1] quantitatively describes how light bends or refracts when transitioning between different optical mediums with varying refractive indices. It defines a mathematical connection between the angles of incidence and refraction. In the context of Snell's Law, the light path between two points is the one that reduces the time needed for light to travel from the source to the observer, considering the changes in the refractive index along the way. Therefore, while Snell's Law quantifies the angle of refraction at the boundary between two mediums, the Fermat principle explains why light follows this particular path by minimizing the time it takes to travel between two points. In media with graded indices, where the refractive index changes spatially, the Fermat principle affects the path of light rays, resulting in curved trajectories explained by Snell's Law.

Figure 1 illustrates the fundamental concept of Snell's law [41]. In graded-index media, the light path bends or refracts by Snell's law. This problem leads to a more complex radiative transfer solution than uniform-index media. Typically, in such instances, the refractive index varies from the center of the material to its surface.

2.1 The model

Radiation transport equation in graded index media

The radiation transport equation for graded-index media, which describes the distribution of radiative intensity $I(s, \Omega, t)$ at position s and time t in the direction $\Omega(\theta, \varphi)$, is given as [47].

$$\frac{n}{c_0} \frac{\partial}{\partial t} I(t, s, \Omega) + (k_e + \Omega \cdot \nabla) I(t, s, \Omega) + \frac{1}{n \sin \theta} \cdot I_\theta + \frac{1}{n \sin \theta} \cdot I_\varphi = \mathcal{S}(t, s, \Omega), \quad (2.1)$$

Where $I_\theta = \frac{\partial}{\partial \theta} \{I(t, s, \Omega)(\Omega \cos \theta - k) \cdot \nabla n\}$ and $I_\varphi = \frac{\partial}{\partial \varphi} \{(s_1 \cdot \nabla n) I(t, s, \Omega)\}$. Here, n , s , and k_e are the refractive index, position vector, and extinction coefficient. $\Omega = i \sin \theta \cos \varphi + j \sin \theta \sin \varphi + k \cos \theta$ is the direction vector, and $s_1 = k \times \frac{\Omega}{|k \times \Omega|} = -i \sin \varphi + j \cos \varphi$, where i , j , and k signify the unit vectors in the coordinate system. The sum of coefficients k_a (absorption) and k_s (scattering) represent extinction coefficients. The sum of k_a and k_s equals the extinction coefficients k_e . The single scattering albedo can be expressed as $\omega = \frac{k_s}{k_e}$. The source term $\mathcal{S}(s, \Omega, t)$ is

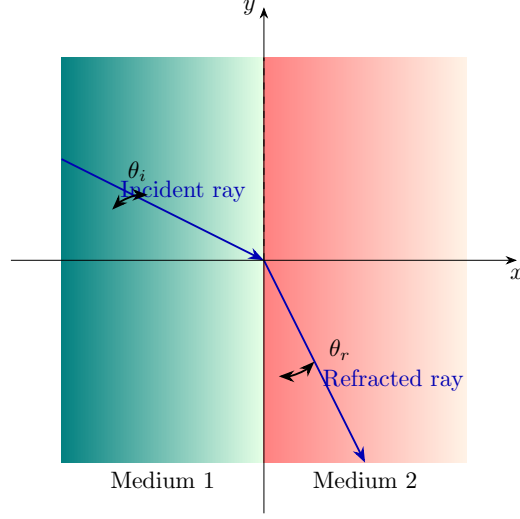


Figure 1: An illustration of a Snell's law.

provided as [47], [44]

$$\mathcal{S}(t, s, \Omega) = n^2 k_a I_b(T_g) + \frac{k_s}{4\pi} \int_{4\pi} \Phi(\Omega' \rightarrow \Omega) I(t, s, \Omega') d\Omega',$$

where T_g denote medium temperature. Scattering phase function $\Phi(\Omega' \rightarrow \Omega)$ describes the energy redistribution from the incoming direction $\Omega'(\theta', \varphi')$ to the outgoing direction $\Omega(\theta, \varphi)$.

Boundary conditions of the model are $\Omega \cdot \hat{n}_\omega < 0$ and $\Omega_{rs} \cdot \hat{n}_\omega < 0$. In this context, \hat{n}_ω is the normal vector that points outward from the surface. The direction $\Omega_{rs} = \Omega - 2(\Omega \cdot \hat{n}_\omega)\hat{n}_\omega$ represents the incident direction for specular reflection. The boundary intensity for $\Omega_{rs} \cdot \hat{n}_\omega < 0$ is

$$I(t, s_\omega, \Omega) = Q_{ext} + \rho_\omega^{spec} I(s_{t,\omega}, \Omega_s) + n_\omega^2 \varepsilon_\omega I_{b\omega} + \frac{\rho_\omega^d}{\pi} \int_{\Omega' \cdot \hat{n}_\omega > 0} |\Omega' \cdot \hat{n}_\omega| I(t, s_\omega, \Omega') d\Omega',$$

Where $I_{b\omega}$ represents the black-body intensity at the boundary, while ρ^{spec} and ρ^d denote the specular and diffuse reflectivities of the boundary, respectively, with emissivity ε_ω . The external driving force Q_{ext} is incoming from the external side of the boundary at a direction Ω_0 as described by Snell's law. From the RTE, the radiative flux vector $q(t, s)$ and the incident radiation $G(t, s)$ at any point $M(x, y)$ can be computed as follows:

$$q(t, s) = \int_{4\pi} \Omega I(t, s, \Omega) d\Omega, \quad G(t, s) = \int_{4\pi} I(t, s, \Omega) d\Omega.$$

Laser irradiation's collimated intensity I_c experiences attenuation as it travels through the medium. This problem can be solved analytically within the medium, with the boundary condition $I_c(t, s_\omega, \Omega) = Q_{ext}$. The reduction in collimated intensity I_c in the medium results in the generation of diffuse intensity $I_d(t, s, \Omega)$. Consequently, the total intensity $I(t, s, \Omega)$ comprises both collimated and diffuse components, expressed as:

$$I(t, s, \Omega) = I_c(t, s, \Omega) + I_d(t, s, \Omega).$$

This equation represents the transport equation for graded-index media and is a fundamental framework for modeling radiation transport in such materials.

2.2 The underlying model and domain

Here, $\Omega \in S, S \subseteq \mathbb{S}^{d-1}$ (sphere), $t \in [0, T]$, position variable $s \in D \subset \mathbb{R}^d$, $D_T = [0, T] \times D$, $I : [0, T] \times D \times S \rightarrow \mathbb{R}$, $k_e = k(s) : D \rightarrow \mathbb{R}_+$, $k_a = k(s) : D \rightarrow \mathbb{R}_+$, $k_s = k(s) : D \rightarrow \mathbb{R}_+$, $\Phi : S \times S \rightarrow \mathbb{R}$.

Here, the above-defined model will be applied to two approaches: the data-driven approach, also known as the forward problem, and the data-driven discovery approach, commonly referred to as data assimilation or the inverse problem.

2.2.1 The underlying model for forward problem

Here, we will define the radiation transport equation with supplemented initial conditions(I.C.) and boundary conditions(B.C.). The defined partial integrodifferential supplied the I.C. and B.C., which are the following:

I.C.

$$I(0, s, \Omega) = I_0(s, \Omega) \quad \text{where } (s, \Omega) \in D \times S, \quad (2.2)$$

And $I_0 : D \times S \rightarrow \mathbb{R}$,

B.C.

$$\beta = \{(t, s, \Omega) \in [0, T] \times \partial D \times S : \Omega \cdot \hat{n}_\omega < 0\}. \quad (2.3)$$

We can wrote $I(t, s, \Omega) = I_b(t, s, \Omega)$ for some B.C, we can wrote $I_b : \beta \rightarrow \mathbb{R}$.

2.2.2 The underlying model for inverse problem

The underlying equation with solution I is considered within the subdomain $D'_T \times S$. This assumption holds that the operator \mathcal{L} applied to I in this region equals a given data g . Mathematically, it can be denoted as:

$$\mathcal{L}(I) = g, \quad \forall (s, \Omega) \in D'_T \times S,$$

Where $D' \subset D$, $D'_T = [0, T] \times D'$ and g is a source term.

2.3 Quadrature rules

Following the approaches outlined in [29–31], let \mathbf{D} represent a domain and ϱ be an integrable function defined as $\varrho : \mathbf{D} \rightarrow \mathbb{R}$. Consider the space-time domain $D_T = [0, T] \times D \subset \mathbb{R}^d$, where $\bar{d} = 2d + 1 \geq 1$. We define a mapping $\varrho : \mathbf{D} \rightarrow \mathbb{R}$, where

$$\varrho = \int_{\mathbf{D}} \varrho(z) dz, \quad (2.4)$$

with dz representing the \bar{d} -dimensional Lebesgue measure. To approximate this integral, we utilize quadrature points $z_i \in \mathbf{D}$ for $1 \leq i \leq N$, along with their corresponding weights w_i . The quadrature approximation of ϱ is expressed as:

$$\varrho_N = \sum_{i=1}^N w_i \varrho(z_i), \quad (2.5)$$

Here, z_i represents the quadrature points. For cases where $\bar{d} \leq 4$, standard composite Gauss quadrature rules can be applied using an underlying grid. The selection of quadrature points and weights depends on the order of the quadrature rule, as outlined in [40]. However, Gauss quadrature becomes inefficient for higher-dimensional domains. In cases of moderate dimensionality ($4 \leq \bar{d} \leq 20$), low-discrepancy sequences, such as Sobol and Halton sequences, are effective for selecting quadrature points, assuming that the function ϱ has a bounded Hardy-Krause variation [6]. In cases of high dimensionality (when $d \gg 20$), Monte Carlo quadrature is the favored approach, exacting randomly chosen quadrature points that are independent and identically distributed(i.i.d.) [6]. Let \mathbf{S} represent a training dataset, and define the space-time domain as $D_T = [0, T] \times D$. The selection of training set $\mathbf{S} \subseteq [0, T] \times D$ will be depend on appropriate quadrature points. For the PINN algorithms, we choose random points $z_i^a = (\Omega_i^{\mathbf{S}})$ for $1 \leq i \leq N_{\mathbf{S}}$, where $w_i^{\mathbf{S}}$ represents the corresponding quadrature weights, and $a \geq 1$. The Quasi-Monte Carlo (QMC) quadrature method remains unaffected by the curse of dimensionality. In situations where the geometry of the domain is particularly intricate, random points can be chosen as training samples, which, i.i.d. according to the underlying uniform distribution.

2.4 Training points

Physics informed neural networks require four types of training points as described in [29, 30]: interior points ζ_{int} , temporal boundary points ζ_{tb} , spatial boundary points ζ_{sb} , and data points $\zeta_{\mathbf{d}}$. Figs.2 and 3 illustrate the training points used in forward and inverse problems (steady state). In Fig. 3 s_1 and s_2 represent spatial position respectively.

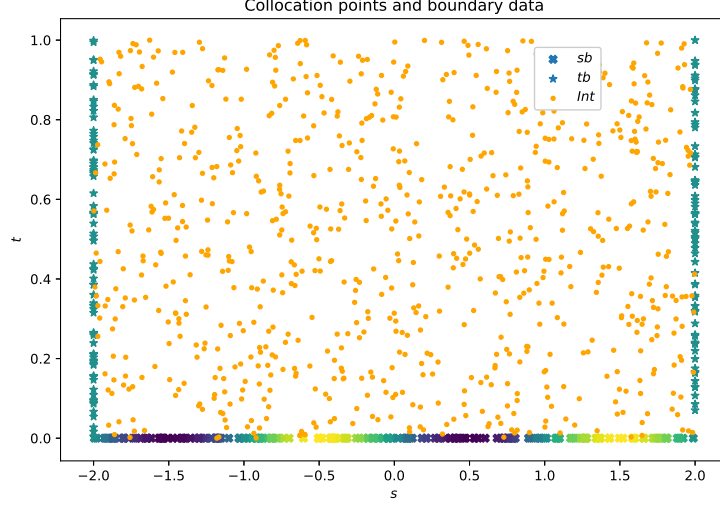


Figure 2: Training points (forward problem): A depiction of the training set \mathcal{S} with randomly selected training points. Yellow dots represent interior points, while green and blue dots indicate the temporal and spatial boundary points.

2.4.1 Interior training points

The interior training points are denoted by $\zeta_{\text{int}} = \{z_j^{\text{int}}\}$ for $1 \leq j \leq N_{\text{int}}$, where $z_j^{\text{int}} = (t_j^{\text{int}}, s_j^{\text{int}}, \Omega_j^{\text{int}})$. Here, $t_j^{\text{int}} \in [0, T]$, $s_j^{\text{int}} \in D$, and $\Omega_j^{\text{int}} \in S$, for all j . These points correspond to quadrature points with weights w_j^{int} based on a suitable quadrature rule. In domains D that are logically rectangular, one can either use Sobol points or randomly select points to create the training set.

2.4.2 Temporal boundary training points

The temporal boundary points are represented as $\zeta_{\text{tb}} = \{z_j^{\text{tb}}\}$, for $1 \leq j \leq N_{\text{tb}}$, with $z_j^{\text{tb}} = (s_j^{\text{tb}}, \Omega_j^{\text{tb}})$. Here, $s_j^{\text{tb}} \in D$, and $\Omega_j^{\text{tb}} \in S$, $\forall j$. The designated points function as quadrature points within an appropriate quadrature rule, accompanied by weights denoted as w_j^{tb} . For logically rectangular domains D , Sobol points can be chosen, or alternatively, random points can be employed to construct the training dataset, similar to the above method.

2.4.3 Spatial boundary training points

The spatial boundary points are denoted as $\zeta_{\text{sb}} = \{z_j^{\text{sb}}\}$, for $1 \leq j \leq N_{\text{sb}}$, where $z_j^{\text{sb}} = (t_j^{\text{sb}}, s_j^{\text{tb}}, \Omega_j^{\text{tb}})$. In this case, $t_j^{\text{sb}} \in [0, T]$, $s_j^{\text{tb}} \in \partial D$, and $\Omega_j^{\text{tb}} \in S$. For logically rectangular domains D , Sobol points can be chosen, or alternatively, random points can be employed to construct the training dataset, similar to the above method.

2.4.4 Data training points

The data training set is defined as $\zeta_{\mathcal{d}} = \{z_j^{\mathcal{d}}\}$ for $1 \leq j \leq N_{\mathcal{d}}$, where $z_j^{\mathcal{d}} \in D' \subset D$.

2.5 Neural networks

The PINN functions as a feed-forward neural network, as illustrated in Fig. 4. A neural network without an activation function behaves as a simple multiple regression model. However, the activation function adds non-linearity, allowing the network to learn and execute more complex tasks. The sigmoid, hyperbolic tangent (tanh), and ReLU functions are some examples of activation functions [17].

The input to the network is $y = (t, s, \Omega) \in \mathcal{D} = [0, T] \times D \times S$. The neural network can be expressed as an affine map:

$$I_{\Theta}(y) = C_K \circ \sigma \circ C_{K-1} \circ \dots \circ \dots \sigma \circ C_1(y). \quad (2.6)$$

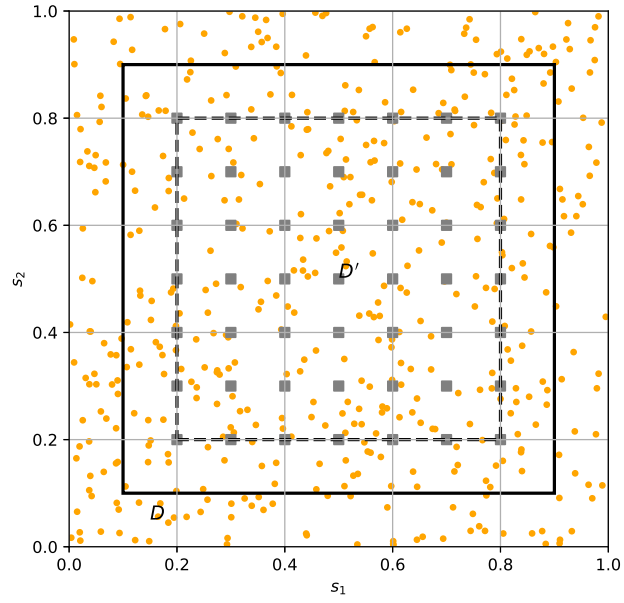


Figure 3: Training points (inverse problem): A representation of the training set \mathcal{S} with randomly selected training points. Yellow dots indicate interior points, and grey dots represent Sobol points.

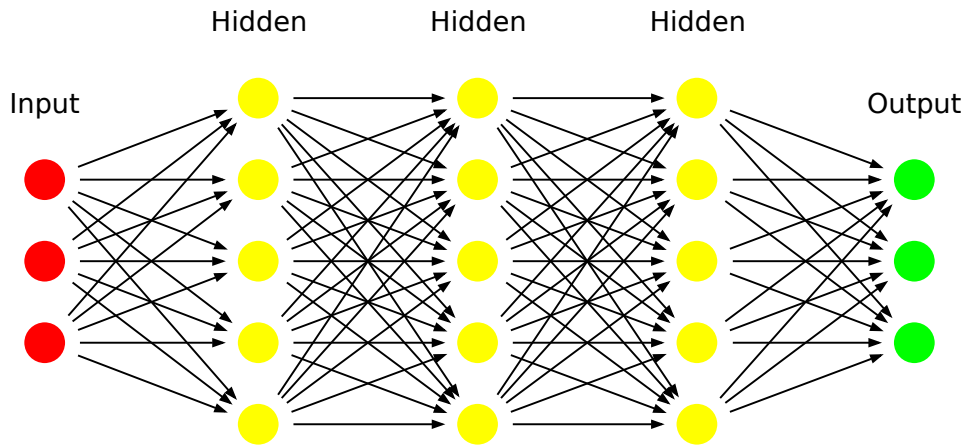


Figure 4: In this diagram, input layer neurons are depicted in red, hidden layer neurons in yellow, and output layer neurons in green.

Where \circ and σ are a composition of functions and activation functions, respectively. For any layer k such that $1 \leq k \leq K$, the transformation at the k -th layer is defined as follows:

$$C_k z_k = W_k z_k + b_k \quad \text{where} \quad W_k \in \mathbb{R}^{d_{k+1} \times d_k}, z_k \in \mathbb{R}^{d_k}, \quad \text{and} \quad b_k \in \mathbb{R}^{d_{k+1}}. \quad (2.7)$$

To ensure consistency, we establish $d_1 = \bar{d} = 2d + 1$, where d represents the spatial dimension, and we define $d_K = 1$ for the output layer. In the context of machine learning, this neural network consists of an input layer, an output layer, and $K - 1$ hidden layers, with the condition that $1 < K < \mathbb{N}$. Each hidden layer k , which consists of d_k neurons, takes an input vector $z_k \in \mathbb{R}^{d_k}$. Initially, this input vector is transformed using the linear mapping C_k , after which it is processed by a non-linear activation function represented as σ . The overall count of neurons in the network can be expressed as $2d + 2 + \sum_{k=2}^{K-1} d_k$. We define the parameter set for the network, which includes weights and biases, as $\Theta = \{W_k, b_k\}$. Furthermore, we denote the set of weights as $\Theta_w = \{W_k\}$ for all $1 \leq k \leq K$ [29, 30]. The parameters Θ lie in the space $\Theta' \subset \mathbb{R}^P$, and P denote total number of parameters:

$$P = \sum_{k=1}^{K-1} (d_k + 1) d_{k+1}. \quad (2.8)$$

2.6 Residuals

This section outlines the residuals associated with the divided training sets, including interior, temporal, data (for inverse), and spatial training points. The focus is on minimizing these residuals. Optimization techniques will involve stochastic gradient descent methods, such as ADAM for first-order optimization, and higher-order approaches like variations of the BFGS algorithm. The PINN I_Θ depends on tuning parameters $\Theta \in \Theta'$, which represent the weights and biases within the network. In a typical deep learning setup, the network is trained by optimizing these parameters Θ to ensure that the neural network approximation I_Θ accurately aligns with the exact solution I . The interior residual can be written as:

$$R_{\text{int}, \Theta} = R_{\text{int}, \Theta}(t, s, \mathbf{\Omega}), \quad \forall (t, s, \mathbf{\Omega}) \in [0, T] \times D \times S, \quad (2.9)$$

We can express the interior residual $R_{\text{int}, \Theta}$ as:

$$\begin{aligned} R_{\text{int}, \Theta} = & \frac{n}{c_0} \frac{\partial}{\partial t} I_\Theta + (k_e + \mathbf{\Omega} \cdot \nabla) I_\Theta + \frac{1}{n \sin \theta} \frac{\partial}{\partial \theta} \{I_\Theta(\mathbf{\Omega} \cos \theta - k) \cdot \nabla n\} \\ & + \frac{1}{n \sin \theta} \frac{\partial}{\partial \varphi} \{(s_1 \cdot \nabla n) I_\Theta\} - n^2 k_a I_{b\Theta}(T_g) - \frac{k_s}{4\pi} \sum_{i=1}^{N_S} w_i^S \Phi(\mathbf{\Omega}, \mathbf{\Omega}_i^S) I_\Theta. \end{aligned} \quad (2.10)$$

In this equation, $(\mathbf{\Omega}_i^S)$ represent the Gauss-Legendre quadrature points, while w_i signify the corresponding quadrature weights of order S . The residuals for the initial, boundary, and data points are defined as follows:

$$\begin{aligned} R_{\text{tb}} &= R_{\text{tb}, \Theta} = I_\Theta - I_0, \quad \forall (s, \mathbf{\Omega}) \in D \times S, \\ R_{\text{sb}} &= R_{\text{sb}, \Theta} = I_\Theta - I_b, \quad \forall (t, s, \mathbf{\Omega}) \in \beta. \end{aligned} \quad (2.11)$$

And

$$R_d = \mathcal{L}(I_\Theta) - g, \quad \forall (s, \mathbf{\Omega}) \in D'_T \times S. \quad (2.12)$$

We aim to find the optimal set of tuning parameters $\Theta \in \Theta'$ that minimizes the residual specified in the forward problem equation,

$$\Theta^* \in \Theta' : \Theta^* = \arg \min_{\Theta \in \Theta'} \left(\|R_{\text{int}, \Theta}\|_{L^2([0, T] \times D \times S)}^2 + \|R_{\text{sb}, \Theta}\|_{L^2(\beta)}^2 + \|R_{\text{tb}, \Theta}\|_{L^2(D \times S)}^2 \right). \quad (2.13)$$

For the inverse problem, we add the term corresponding to the data residual R_d to Eq.(2.13). This results in the following minimization problem:

$$\Theta^* \in \Theta' : \Theta^* = \arg \min_{\Theta \in \Theta'} \left(\|R_{\text{int}, \Theta}\|_{L^2(D_T \times S)}^2 + \|R_{\text{sb}, \Theta}\|_{L^2(\beta)}^2 + \|R_{d, \Theta}\|_{L^2(D'_T \times S)}^2 \right). \quad (2.14)$$

The integrals in Eqs.(2.13) and (2.14) cannot be calculated exactly due to the use of the L^2 norm, necessitating approximation through an appropriate quadrature method.

2.7 Loss functions and optimization

We approximate the above integral with the following loss functions for forward and inverse problems, respectively

$$\mathcal{J}_1(\Theta) = \sum_{j=1}^{N_{sb}} w_j^{sb} |\mathbf{R}_{sb,\Theta}(z_j^{sb})|^2 + \sum_{j=1}^{N_{tb}} w_j^{tb} |\mathbf{R}_{tb,\Theta}(z_j^{tb})|^2 + \lambda \sum_{j=1}^{N_{int}} w_j^{int} |\mathbf{R}_{int,\Theta}(z_j^{int})|^2, \quad (2.15)$$

$$\mathcal{J}_2(\Theta) = \sum_{j=1}^{N_d} w_j^d |\mathbf{R}_{d,\Theta}(z_j^d)|^2 + \sum_{j=1}^{N_{sb}} w_j^{sb} |\mathbf{R}_{sb,\Theta}(z_j^{sb})|^2 + \lambda \sum_{j=1}^{N_{int}} w_j^{int} |\mathbf{R}_{int,\Theta}(z_j^{int})|^2, \quad (2.16)$$

Regularize the minimization problems for the loss function, i.e

$$\Theta^* = \arg \min_{\Theta \in \Theta'} (\mathcal{J}_i(\Theta) + \lambda_{reg} \mathcal{J}_{reg}(\Theta)), \quad (2.17)$$

Where $i = 1, 2$. In machine learning, it is common to incorporate a regularization term to mitigate overfitting. A widely used form of the regularization function is $\mathcal{J}_{reg}(\Theta) = \|\Theta\|_q^q$, where q is typically 1 (for L^1 regularization) or 2 (for L^2 regularization). The parameter λ_{reg} controls the balance between the regularization term and the actual loss function \mathcal{J} , with $0 \leq \lambda_{reg} \ll 1$. Stochastic gradient descent methods, including ADAM, will be applied due to their popularity in first-order optimization. Additionally, advanced optimization techniques, including various forms of the BFGS algorithm, may be employed. Our aim is to identify the optimal solution $I^* = I_{\Theta^*}$ using the training sets. We begin with an initial value $\bar{\Theta} \in \Theta'$ and calculate the network output $I_{\bar{\Theta}}$, PDE residual, boundary residual, loss function, and its gradients. Ultimately, the optimal solution is $I^* = I_{\Theta^*}$, which is determined by the PINN.

We approximate local minimum in (2.17) as Θ^* . The resulting DNNs $I^* = I_{\Theta^*}$ will solution I of (2.1). The Table1 contains a hyperparameter of numerical experiments. We summarize the PINN algorithms for approximating RTE in a graded index medium. The algorithms are described in [29], [30], [2], and [31]. Below, Algorithm 2.1 is presented for forward problems, while Algorithm 2.2 addresses inverse problems:

Table 1: The configurations of hyperparameters and the frequency of retraining utilized in ensemble training for physics-informed neural networks (PINN).

Examples	$K - 1$	\bar{d}	λ	λ_{reg}	n_{Θ}
Example 1a,b,c	4, 8	20, 24	0.1, 1, 10	0	4
Example 2a,b,c,d	4, 8	24, 28	0.1, 1, 10	0	10,10,4,4
Example 3a,b,c	4, 8	24, 28	0.1, 1, 10	0	4
Example 4a, b	4, 8	20, 24	0.1, 1, 10	0	4
Example 5a,b,c	4, 8	20, 24	0.1, 1, 10	0	4
Example 6a, b	4, 8	20, 24	0.1, 1, 10	0	4,5

Algorithm 2.1. Algorithm for developing a PINN to estimate radiative intensity in forward problems.

Inputs: Underlying domain, data, and coefficients for the RTE with graded index Eq.(2.1); quadrature points and weights for the underlying quadrature rules; non-convex gradient-based optimization algorithms.

Aim: To approximate the solution of the model, using a PINN $I^* = I_{\Theta^*}$.

Step 1: Select the training sets as outlined in section 2.4.

Step 2: Initialize with a weight vector $\bar{\Theta} \in \Theta'$ and calculate: neural network $I_{\bar{\Theta}}$ Eq.(2.6), PDE residual Eq.(2.10), boundary residuals Eq.(2.11), loss function Eq.(2.15), Eq.(2.17), and gradients for optimization algorithm initiation.

Step 3: Execute the optimization algorithm until reaching an approximate local minimum Θ^* of Eq.(2.17). The resulting function $I^* = I_{\Theta^*}$ is the desired PINN for approximating the radiative transfer equation solution I .

2.8 Estimation on generalization error

Let the spatial domain be $D = [0, 1]^d$, where d denote the spatial dimension. This section focuses on obtaining an accurate estimation of the generalization error or so-called total error for the trained neural network, $I^* = I_{\Theta^*}$. This result arises from the application of the PINNs algorithms 2.1 and 2.2. The error can be expressed as follows:

$$E_G = E_G(\theta^*) = \left(\int_{\mathcal{D}} |I(t, s, \Omega) - I^*(t, s, \Omega)|^2 dX \right)^{\frac{1}{2}} \quad (2.18)$$

Where $dX = dt ds d\Omega$ denotes the volume measure on \mathcal{D} . This approach outlined in [29], [2], [30], and [31]. This section provides an estimation of the generalization error, as defined in equation (2.18), based on the training error.

$$\begin{aligned} E_T^{N_{sb}} &= \left(\sum_{j=1}^{N_{sb}} w_j^{sb} |R_{sb, \Theta^*}(z_j^{sb})|^2 \right)^{\frac{1}{2}}, E_T^{N_{tb}} = \left(\sum_{j=1}^{N_{tb}} w_j^{tb} |R_{tb, \Theta^*}(z_j^{tb})|^2 \right)^{\frac{1}{2}}, \\ E_T^{N_{int}} &= \left(\sum_{j=1}^{N_{int}} w_j^{int} |R_{int, \Theta^*}(z_j^{int})|^2 \right)^{\frac{1}{2}}, E_T^{N_d} = \left(\sum_{j=1}^{N_d} w_j^d |R_{d, \Theta^*}(z_j^d)|^2 \right)^{\frac{1}{2}}. \end{aligned} \quad (2.19)$$

The generalized error is similar to the form presented in [29] and is expressed as:

$$\begin{aligned} (E_G)^2 &\leq V \left((E_T^{tb})^2 + v(E_T^{sb})^2 + c(E_T^{int})^2 \right) \\ &+ VV_2 \left(\frac{(\log(N_{tb}))^{2d}}{N_{tb}} + c \frac{(\log(N_{sb}))^{2d}}{N_{sb}} + c \frac{(\log(N_{int}))^{2d+1}}{N_{int}} + cN_S^{-2a} \right). \end{aligned} \quad (2.20)$$

Where V_2, v , and V are constants as defined in Appendix D.1.

Consider Φ is symmetric such that

$$\Phi(\Omega, \Omega') = \Phi(\Omega', \Omega),$$

And let

$$\Sigma_g(\Omega) = \int_{4\pi} \Phi(\Omega, \Omega') d\Omega'$$

Where $S \in \Omega'$ and Σ_g is essentially bounded i.e $\Sigma_g \in L^\infty(S)$.

Algorithm 2.2. Algorithm for developing a PINN to estimate radiative intensity in inverse problems.

Inputs: Underlying domain, data, and coefficients for the RTE with graded index Eq.(2.1); appropriate quadrature points and weights for the underlying quadrature rules; and non-convex gradient-based optimization algorithms.

Aim: To approximate the solution I of Eq.(2.1) for inverse problems, using a PINN $I^* = I_{\Theta^*}$.

Step 1: Select the training sets outline in Section 2.4.

Step 2: Initialize with a weight vector $\bar{\Theta} \in \Theta'$ and calculate: neural network $I_{\bar{\Theta}}$ Eq.(2.6), PDE residual Eq.(2.10), data residuals Eq.(2.12), loss function Eq. (2.16), Eq.(2.17) and gradients for optimization algorithm initiation.

Step 3: Execute the optimization algorithm until reaching an approximate local minimum Θ^* of Eq.(2.17). The resulting function $I^* = I_{\Theta^*}$ is the desired PINN for approximating the radiative transfer equation solution I .

2.9 Steady case

If $c_0 \rightarrow \infty$, Eq.(2.1) becomes

$$(k_e + \Omega \cdot \nabla)I + \frac{1}{n \sin \theta} \cdot I_\theta + \frac{1}{n \sin \theta} \cdot I_\varphi = \mathcal{S}, \quad (2.21)$$

B.C.

$$\beta_o = \{(s, \Omega) \in \partial D \times S : \Omega \cdot \hat{n}_\omega < 0\}, \quad (2.22)$$

We can write $I(s, \Omega) = I_b(s, \Omega, \xi)$ for some B.C., we can write $I_b : \beta_o \rightarrow \mathbb{R}$. Let $D = [0, 1]^d$, where d denotes spatial dimension. This section aims to derive a precise generalization error estimate for the trained neural network $I^* = I_{\Theta^*}$. This network is the result of the PINNs algorithms described in algorithms 2.1 and 2.2.

$$E_{G_{steady}} = E_G(\theta^*) = \left(\int_{D \times S} |I(s, \Omega) - I^*(s, \Omega)|^2 dX \right)^{\frac{1}{2}}, \quad (2.23)$$

Where $dX = dsd\Omega$,

$$\begin{aligned} E_T^{N_{sb}} &= \left(\sum_{j=1}^{N_{sb}} w_j^{sb} \left| R_{sb, \Theta^*}(z_j^{sb}) \right|^2 \right)^{\frac{1}{2}}, E_T^{N_{int}} = \left(\sum_{j=1}^{N_{int}} w_j^{int} \left| R_{int, \Theta^*}(z_j^{int}) \right|^2 \right)^{\frac{1}{2}}, \\ E_T^{N_d} &= \left(\sum_{j=1}^{N_d} w_j^d \left| R_{d, \Theta^*}(z_j^d) \right|^2 \right)^{\frac{1}{2}}. \end{aligned} \quad (2.24)$$

The generalized error is similar to the form presented in [29] and is expressed as:

$$\begin{aligned} (E_{G_{steadyf}})^2 &\leq V \left(v(E_T^{sb})^2 + v(E_T^{int})^2 \right) \\ &+ V \left(\frac{(\log(N_{sb}))^{2d}}{N_{sb}} + v \frac{(\log(N_{int}))^{2d}}{N_{int}} + v N_S^{-2a} \right), \end{aligned} \quad (2.25)$$

Where v and V are constants as defined in Appendix D.2.

The generalization error bound expresses that the approximation error for the underlying problems using a trained PINN will remain small if certain conditions are satisfied:

Remark 2.3. The PINN should be effectively trained, as evidenced by a sufficiently small training error. Although the training error cannot be controlled *a priori*, it can be computed *a posteriori*. Sufficient training (collocation) points are required to ensure accurate learning. The quadrature error, which depends on the number of collocation points N and the quadrature constants, can be reduced by selecting a large enough N . This finding underscores that the generalization error estimate sets an upper bound on the total error, encompassing both training errors (from equations 2.19 and 2.24) and the number of training data points N_{int}, N_{sb}, N_{tb} , as well as the quadrature points N_S utilized to approximate the scattering integral (from equation 2.1). Although no *a priori* estimate is available for the training errors, they can be computed after complete training. Therefore, the theorems suggest that the model will provide less relative error if the involved constants remain finite and the PINN is trained adequately. This theory aligns with general machine learning theory, where a well-trained and regularized PINN I^* ensures stability and bounded generalization error. Here $N_{int} > 128$, and $N_{sb, tb} > 64$. ■

Remark 2.4. We address the following inverse problem: suppose that the boundary conditions in equations (2.1) and (2.21), which may also include initial conditions, are unknown. This problem is linked to the PDE being an ill-posed problem. However, we assume noiseless measurements of the underlying solution I are available within a subdomain $D' \subset D$. In most cases, PINNs achieve minimal errors with less than one minute of training time. Due to their simplicity and efficiency, PINNs provide an attractive alternative to current data assimilation methods, particularly in high-dimensional problems. ■

The error estimate primarily relates the overall generalization error to the training error. It uses the stability of the PDE to establish an upper bound based on the PDE residual, which is influenced by both training and quadrature errors. As long as the training errors remain independent of the underlying dimensionality, the above estimate implies that the PINNs described in Algorithms 2.1 and 2.2 will not be impacted by the curse of dimensionality.

3 Numerical experiments

The PINN algorithms 2.1 and 2.2 were implemented using the PyTorch framework [33]. All numerical experiments were performed on an Apple MacBook with an M3 chip and 24 GB of RAM. Several key hyperparameters are essential to the PINNs framework, including the quantity of hidden layers $K - 1$, layer width, selected activation function σ , parameter λ in the loss function, regularization parameter λ_{reg} in the cumulative loss, and the specific gradient descent optimization algorithm. For the activation function σ , we select the hyperbolic tangent (\tanh), which ensures the smoothness properties required by theoretical guarantees for the neural networks are obtained. We employ the second-order LBFGS optimizer to improve convergence. For fine-tuning the remaining hyperparameters, we adopt the ensemble training method described in [2], [29], [30] and [31]. This method involves evaluating different values for the number of hidden layers, layer depth, parameter λ , and regularization term λ_{reg} , as illustrated in Table 1. Each hyperparameter set is used to retrain the model n_θ times in parallel with different random weight initializations. The configuration yielding the lowest training loss is then selected as the best model.

3.1 Forward problem: data driven

3.1.1 Radiation distribution of 1D infinite wall with Gaussian source

This model is based on a non-scattering medium situated between 1D infinite parallel black walls. The model contains Gaussian source term. We assume a constant extinction coefficient for the medium. The following radiative transfer equation describes this problem [24]:

$$\mu \frac{dI}{dx} + k_e I = \exp\left(-(x-c)^2/\alpha^2\right), \quad x, c \in [0, 1] \quad (3.1)$$

The boundary conditions are:

$$I(0, \mu) = k_e^{-1} \exp\left(-c^2/\alpha^2\right), \quad \mu > 0 \quad (3.2a)$$

$$I(1, \mu) = k_e^{-1} \exp\left(-(1-c)^2/\alpha^2\right), \quad \mu < 0 \quad (3.2b)$$

The analytical solution (for $\mu > 0$) is provided as:

$$I(x, \mu) = I(0, \mu) \exp\left(-\frac{k_e x}{\mu}\right) - \frac{\alpha\sqrt{\pi}}{2\mu} \exp\left\{-\frac{k_e}{\mu} \left[x - \left(\frac{\alpha^2 k_e}{4\mu} + c\right)\right]\right\} \\ \times \left[\operatorname{erf}\left(-\frac{k_e \alpha}{2\mu} + \frac{c-x}{\alpha}\right) - \operatorname{erf}\left(-\frac{k_e \alpha}{2\mu} + \frac{c}{\alpha}\right) \right]. \quad (3.3)$$

In this scenario, $\alpha = 0.02$, $c = 0.5$, and $\mu = 0.5$. We compare the radiation intensity distributions calculated for

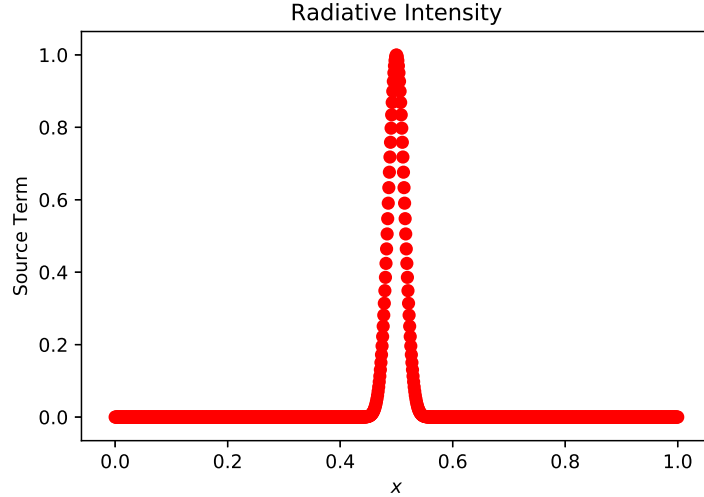


Figure 5: Source term of Eq.3.1.

the direction $\mu = 0.5$ across media with varying extinction coefficients: $k_e = 0.1$, $k_e = 1$, and $k_e = 10 m^{-1}$. Figure 5 represents the source term of the model. The predicted and exact solutions of the RTE for $k_e = 0.1$, $k_e = 1$, and $k_e = 10 m^{-1}$ are presented in Figures 6, 7, and 8, respectively.

The PINN solution is consistent and closely aligned with the exact solutions for all three scenarios. Table 2 demonstrates that the errors remain minimal, further highlighting the PINN's capability to approximate the PDE with low computational cost accurately. The authors simulated the model's relative error for parameters $\mu = 0.5$, $\alpha = 0.02$, and $c = 0.5$. For the meshfree method by Zhao et al. [50], the relative error at $k_e = 0.1, 1$, and $10 m^{-1}$, with meshes ranging from 10 to 400, decreases from 21.77 to 1.95×10^{-3} , 6.35 to 0.36×10^{-2} , and 2.29 to 0.49×10^{-2} , respectively. For the DFEM [14], the relative error at $k_e = 0.1, 1$, and $10 m^{-1}$, with meshes ranging from 10 to 400, reduces from 1.95 to 3.49×10^{-4} , 2.05 to 5.09×10^{-4} , and 1.74 to 0.15×10^{-2} , respectively. For the generalized lattice Boltzmann method, with meshes between 20 and 200, the relative error at $k_e = 0.1, 1$, and $10 m^{-1}$ decreases from 1.6×10^{-2} to 8.9×10^{-5} , 7.4×10^{-2} to 5.3×10^{-4} , and 1.86 to 0.32×10^{-4} , respectively. In contrast, the PINN method achieves a relative L^2 error of 6.4×10^{-4} at $k_e = 10 m^{-1}$.

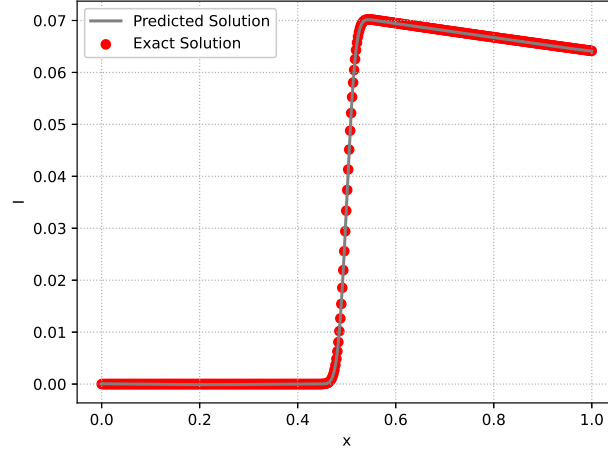


Figure 6: Radiation distribution with a Gaussian source at an extinction coefficients $k_e = 0.1 m^{-1}$.

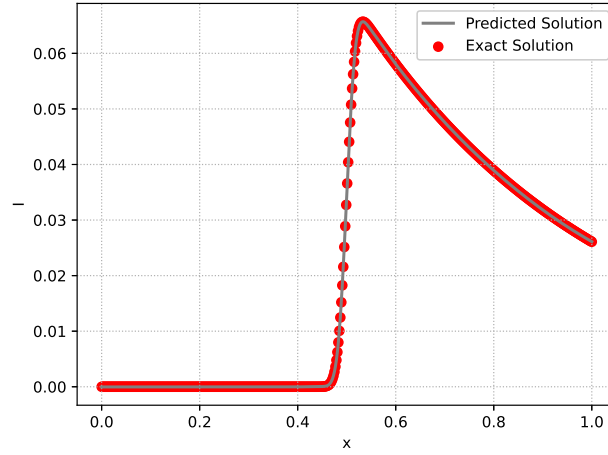


Figure 7: Radiation distribution with a Gaussian source at an extinction coefficients $k_e = 1 m^{-1}$.

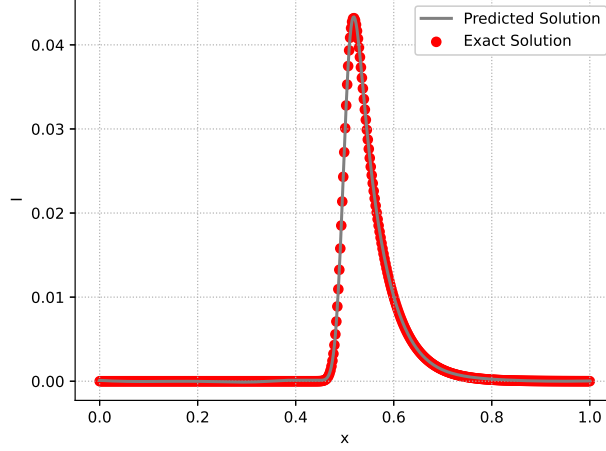


Figure 8: Radiation distribution with a Gaussian source at an extinction coefficients $k_e = 10m^{-1}$.

Case	N_{int}	N_{sb}	$K - 1$	\bar{d}	λ	E_T	$\ I - I^*\ _{L^2}$	Training Time (sec.)
1	8192	4096	4	20	0.1	0.0001	4.24e-05	23
2	8192	4096	4	20	1	0.0002	3.77e-05	16
3	8192	4096	4	20	0.1	0.0008	4.09e-05	30

Table 2: Results for the 1D infinite wall with a Gaussian source term.

3.1.2 Infinite wall with discontinuous source term

In this section, we have presented a new model for the radiation transfer equation in graded-index media. Several types of deficiencies arise with traditional methods like the LSFEM and generalized GFEM, as noted in [49]. This model investigates heat transfer through radiation in an infinite slab with discontinuous source term. For this scenario, the exact analytical solution is provided as

$$I(x, \mu) = \mathbf{1}_{(x-0.5L)} \exp(-k_e(x-0.5L)) + \mathbf{1}_{(0.5L-x)}. \quad (3.4)$$

In this equation, the constant parameter k_e indicates the strength of extinction, while L represents the thickness of the slab. The unit step function is denoted by $\mathbf{1}_{[\cdot]}$. The medium is homogeneous, and the walls are considered black. The source term can easily be derived from an exact solution.

The radiation intensity distributions solved for the direction $\mu = 1$ and $L = 10$ are compared across media with varying extinction coefficients: $k_e = 0.1m^{-1}$, $k_e = 1m^{-1}$, $k_e = 2m^{-1}$, and $k_e = 10m^{-1}$. The boundary conditions of walls are unity. The predicted and exact solutions of the RTE are illustrated in Figures 9, 10, 11, and 12 for $k_e = 0.1m^{-1}$, $k_e = 1m^{-1}$, $k_e = 2m^{-1}$, and $k_e = 10m^{-1}$, respectively. The results obtained from the PINN demonstrate stability and agreement with the exact solutions across all four scenarios. Table 3 shows that errors remain low at both boundaries, demonstrating the PINN's capability to approximate the PDE with minimal computational effort accurately.

Case	N_{int}	N_{sb}	$K - 1$	\bar{d}	λ	E_T	$\ I - I^*\ _{L^2}$	Training Time (sec.)
1	8192	4096	8	24	0.1	0.0005	0.00010	22
2	8192	4096	8	24	0.1	0.0012	0.0004	18
3	8192	4096	8	24	0.1	0.0020	0.0005	19
4	8192	4096	8	24	1	0.009	0.0009	26

Table 3: Results for the radiation transport equation with an infinite wall with discontinuous source.

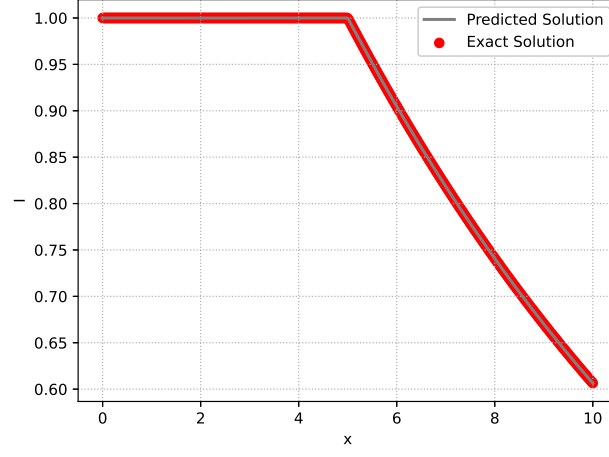


Figure 9: Radiation intensity distributions for an infinite wall with a discontinuous source, comparing results from the exact solution and the PINN method at $k_e = 0.1m^{-1}$.

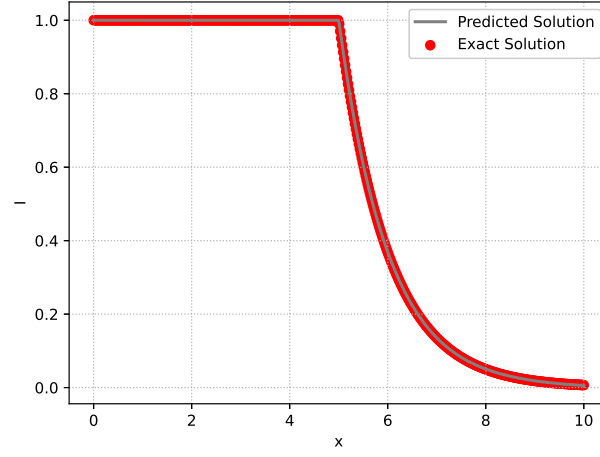


Figure 10: Radiation intensity distributions for an infinite wall with a discontinuous source, comparing results from the exact solution and the PINN method at an extinction coefficient of $k_e = 1m^{-1}$.

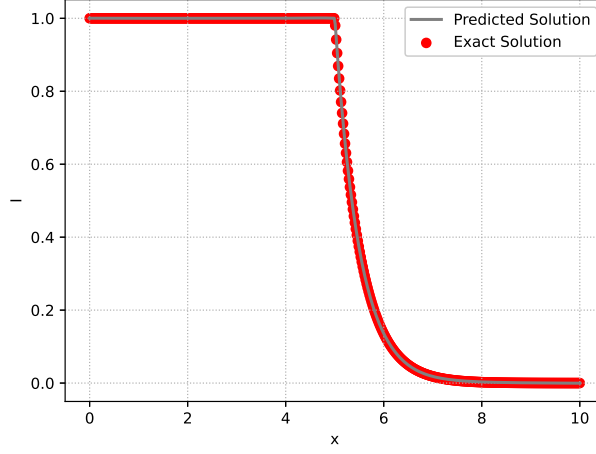


Figure 11: Radiation intensity distributions for an infinite wall with a discontinuous source, comparing results from the exact solution and the PINN method at an extinction coefficient of $k_e = 2m^{-1}$.

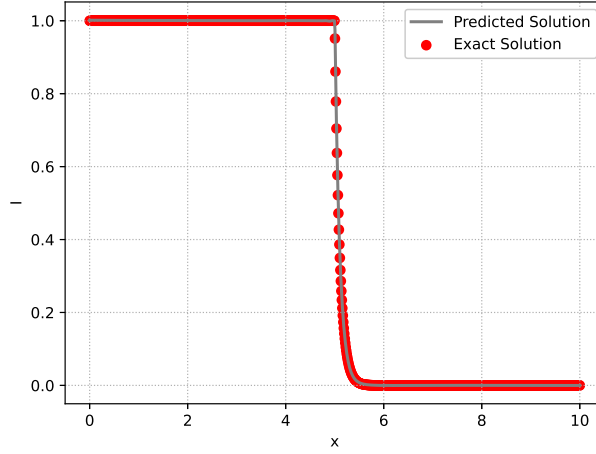


Figure 12: Radiation intensity distributions for an infinite wall with a discontinuous source, comparing results from the exact solution and the PINN method at an extinction coefficient of $k_e = 10m^{-1}$.

3.1.3 Square enclosure radiative distribution with discontinuous source along the diagonal

This section presents a new model for the radiation transfer equation in a square enclosure. A 2D RTE problem is analyzed in this scenario. Figure 13 shows the layout of the square medium. An exact solution exists for this configuration is

$$I(x, y, \mu) = \mathbf{1}_{(x+y-L)} \exp \left[-k_e \frac{x+y-L}{\sqrt{2}} \right] + \mathbf{1}_{(L-x-y)}, \quad x, y \in [0, L]^2 \quad (3.5)$$

In this equation, k_e denotes the extinction strength, $\mathbf{1}_{[\cdot]}$ represents the unit step function. Let the direction Ω be $\left[\frac{1}{\sqrt{2}}, \frac{1}{\sqrt{2}} \right]$ for an enclosure with a side length of $L = 1$. The left and bottom walls have boundary conditions with an intensity of one. The source term can easily be derived from an exact solution. Figures 14, 15, and 16 present the predicted and exact solutions of the RTE for $k_e = 1m^{-1}$, $k_e = 5m^{-1}$, and $k_e = 10m^{-1}$, respectively. As illustrated in Table 4, the errors remain negligible at both boundaries, further showcasing the PINN's ability to accurately model the PDE while maintaining low computational expenses. We also present 3D plots in Figures 17, 18, and 19, which display the exact and predicted solutions of the RTE for $k_e = 1m^{-1}$, $k_e = 5m^{-1}$, and $k_e = 10m^{-1}$, respectively.

Case	N_{int}	N_{sb}	$K - 1$	\bar{d}	λ	E_T	$\ I - I^*\ _{L^2}$	Training Time (sec.)
1	8192	4096	8	28	1	0.007	0.00056	18
2	8192	4096	8	28	1	0.0098	0.00048	19
3	8192	4096	8	28	1	0.020	0.00059	20

Table 4: Results for square medium radiative transfer along the diagonal.

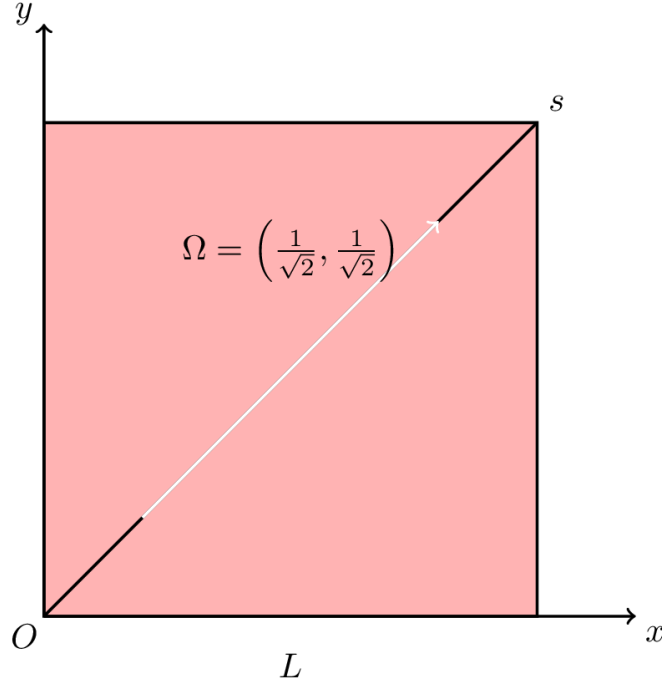


Figure 13: Schematic of the square solution domain.

3.1.4 2D radiation distribution with Gaussian source term

This model is based on an exponential square enclosure. This test represents the 2D form of Eq. (3.1). The radiation transport equation can be modeled as

$$\mu \frac{dI}{dx} + \eta \frac{dI}{dy} + k_e I = \exp \left(-\frac{\left(\frac{x+y}{\sqrt{2}} - c \right)^2}{\alpha^2} \right), \quad x, y \in [0, 1] \quad (3.6)$$

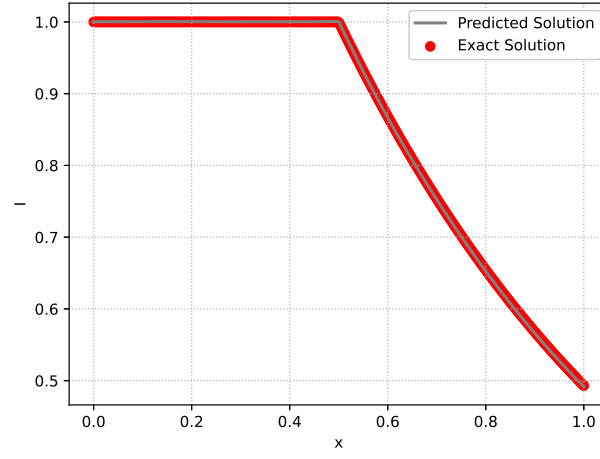


Figure 14: Radiation distribution along the diagonal at extinction coefficients $k_e = 1 m^{-1}$.

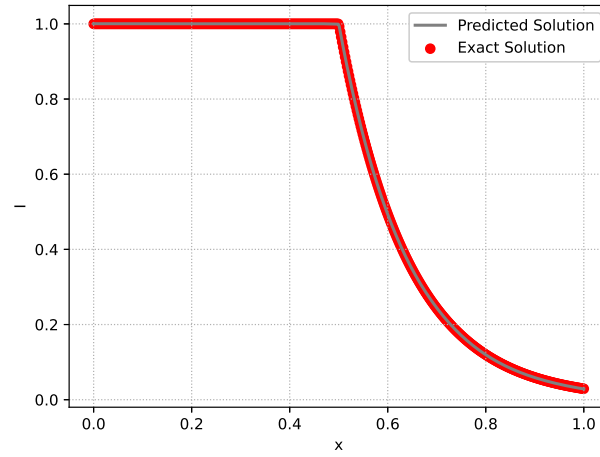


Figure 15: Radiation distribution along the diagonal at extinction coefficients $k_e = 5 m^{-1}$.

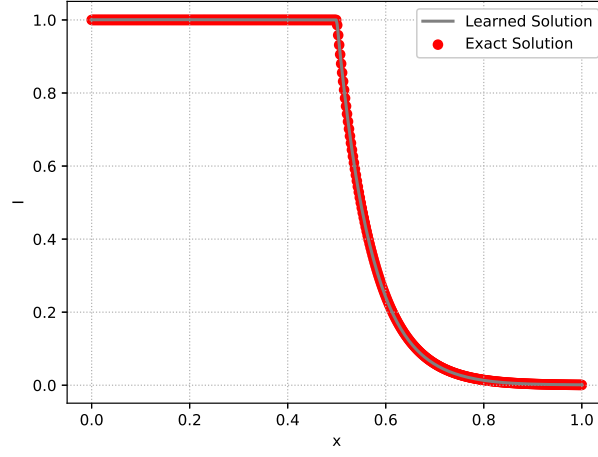


Figure 16: Radiation distribution along the diagonal at extinction coefficients $k_e = 10m^{-1}$.

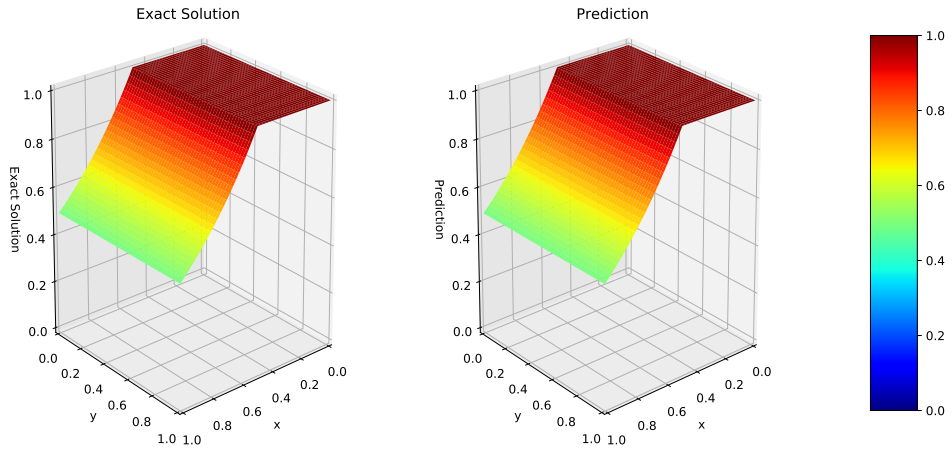


Figure 17: 3D plot for radiation distribution along the diagonal at extinction coefficients $k_e = 1m^{-1}$.

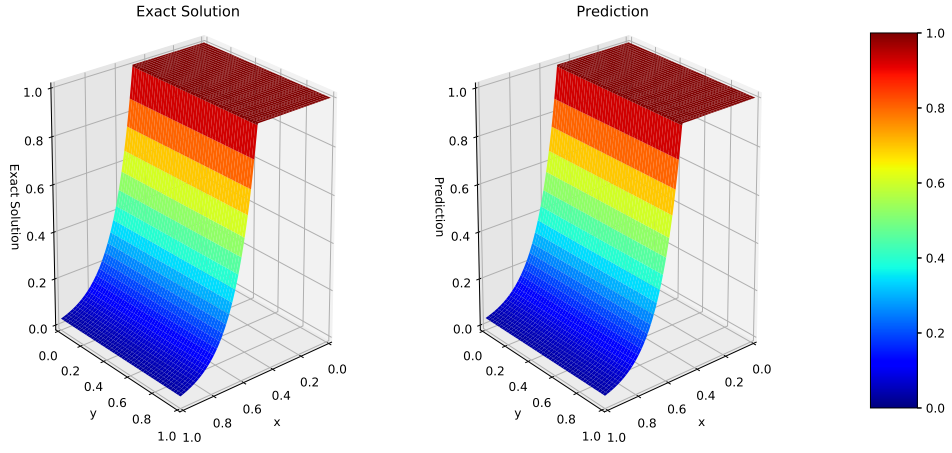


Figure 18: 3D plot for radiation distribution along the diagonal at extinction coefficients $k_e = 5m^{-1}$.

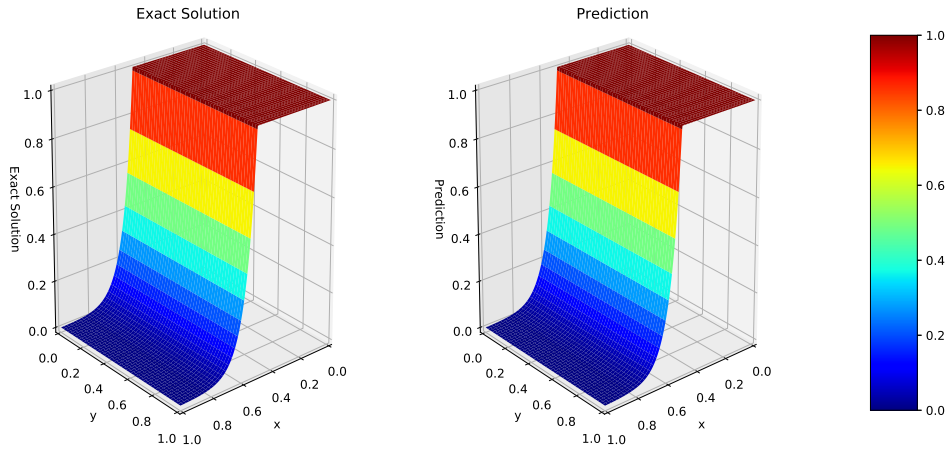


Figure 19: 3D plot for radiation distribution along the diagonal at extinction coefficients $k_e = 10m^{-1}$.

Let the incident direction be defined as $\mu = \frac{\sqrt{2}}{2}$, $\eta = \frac{\sqrt{2}}{2}$ and $c = \frac{\sqrt{2}}{2}$. The analytical solution [50] is

$$I(x, y) = \frac{\alpha\sqrt{\pi}}{2} \exp \left\{ -k_e \left[\frac{|x+y|-|x-y|}{\sqrt{2}} - \frac{1-|x-y|}{\sqrt{2}} - \frac{\alpha^2 k_e}{4} \right] \right\} \times \left[\operatorname{erf} \left(\frac{\alpha k_e}{2} + \frac{1-|x-y|}{\sqrt{2}\alpha} \right) - \operatorname{erf} \left(\frac{\alpha k_e}{2} + \frac{\frac{|x+y|-|x-y|}{\sqrt{2}} - \frac{1-|x-y|}{\sqrt{2}}}{\alpha} \right) \right] \quad (3.7)$$

Fig. 20 illustrates the source term in Eq.(3.6). Figs. 21, and 22 depict both the exact and predicted solutions of the RTE for $k_e = 0.1m^{-1}$ and $k_e = 1m^{-1}$ respectively. The errors, as presented in Table 5, are minimal, further highlighting the ability of the PINN with minimal computational effort accurately. At $k_e = 1m^{-1}$, the relative average error of the meshfree method [50] is 0.7. The relative error of the MRT lattice Boltzmann method [15] at $k_e = 1m^{-1}$ is 2.5%. [46] simulated the same model using the lattice Boltzmann method and compared the results with the GFEM. Both [46] and [50] showed that for small values of k_e , the GFEM and the meshfree method, respectively, performed poorly.

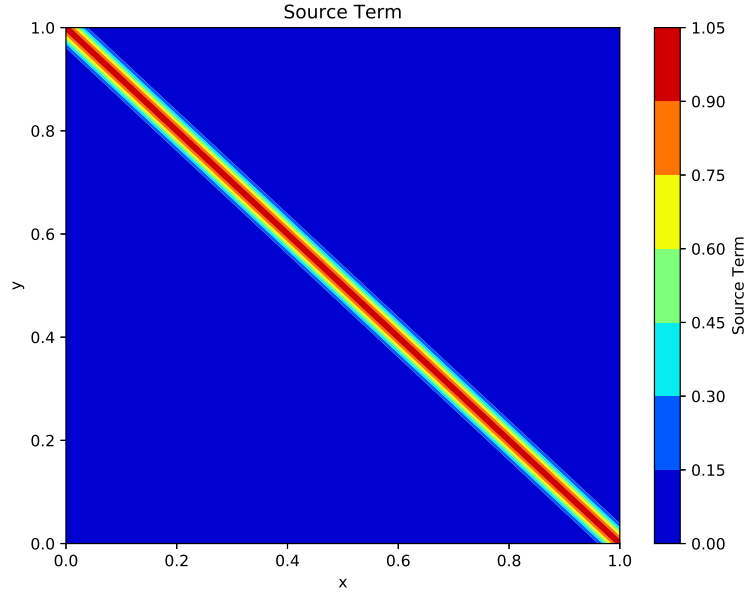


Figure 20: Source term at x is not equal to y .

Case	N_{int}	N_{sb}	$K - 1$	\bar{d}	λ	E_T	$\ I - I^*\ _{L^2}$	Training Time (sec)
1	8192	4096	4	20	0.1	0.0008	0.04	31
2	8192	4096	4	20	0.1	0.0009	0.05	27

Table 5: Results for 2D Radiation distribution with a Gaussian source(forward).

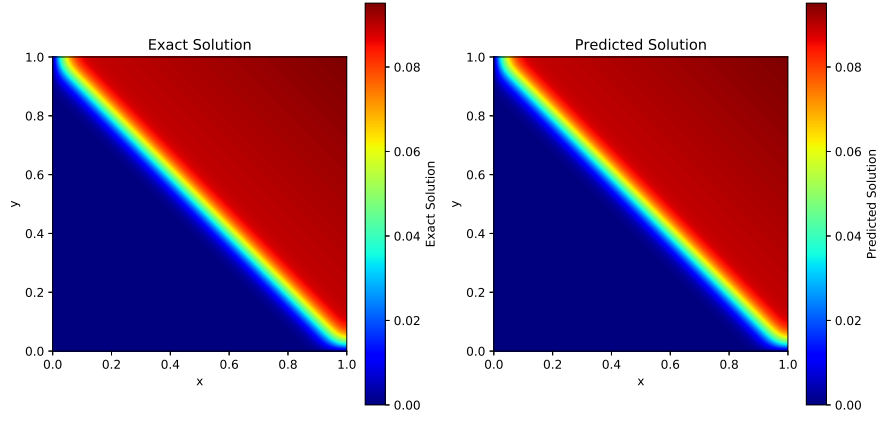


Figure 21: 2D Radiation distribution with a Gaussian source, solved by PINN and exact at $k_e = 0.1m^{-1}$.

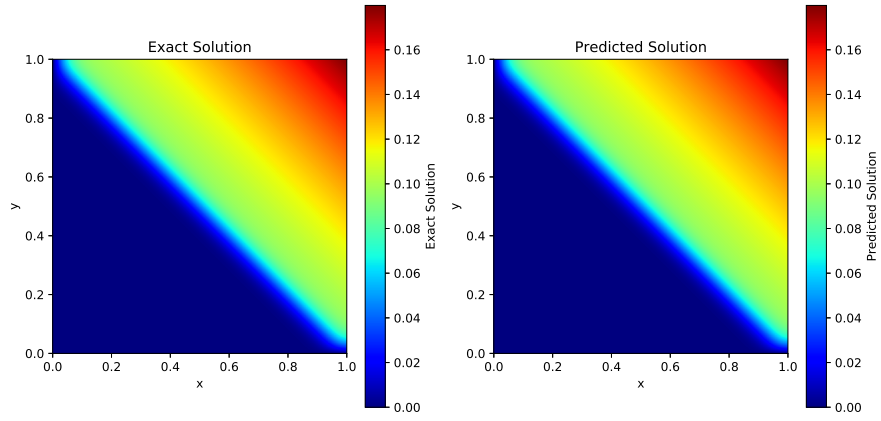


Figure 22: 2D Radiation distribution with a Gaussian source, solved by PINN and exact at $k_e = 1m^{-1}$.

3.1.5 Radiation distribution with a Gaussian source field along diagonal

The numerical experiment discussed in Section (3.1.4) is conducted under the condition $x = y$ with black and cold boundary conditions. A PINN determines the radiation distribution along the square enclosure's diagonal ($y = x$). Figure 23 represents the source term. Figures 24, 25, and 26 illustrate exact and predicted solutions of the RTE for $k_e = 0.1m^{-1}$, $k_e = 1m^{-1}$, and $k_e = 2m^{-1}$, respectively. As shown in Table 6, the errors are minimal at both boundaries, further demonstrating the PINN's capability to approximate the PDE with low computational cost accurately.

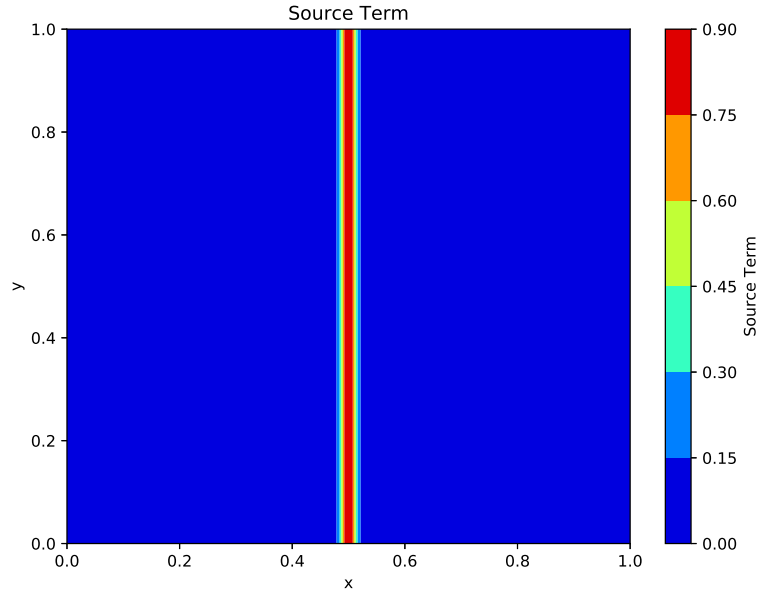


Figure 23: Source term at $x = y$.

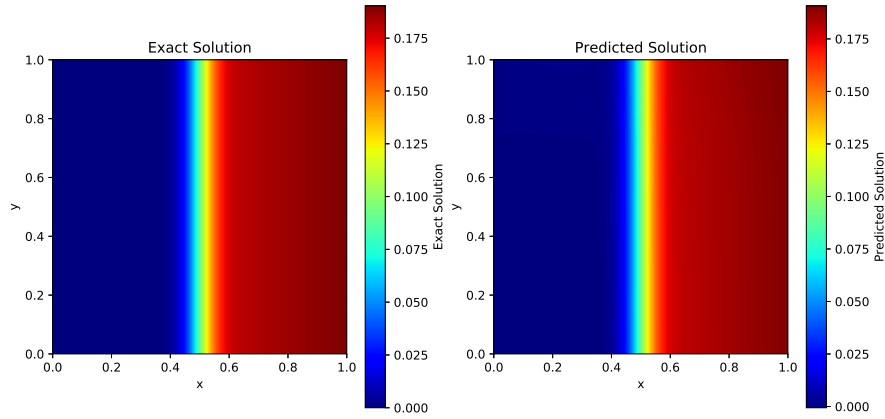


Figure 24: Radiation distribution with a Gaussian source, solved by PINN and exact at $k_e = 0.1m^{-1}$ for $x = y$.

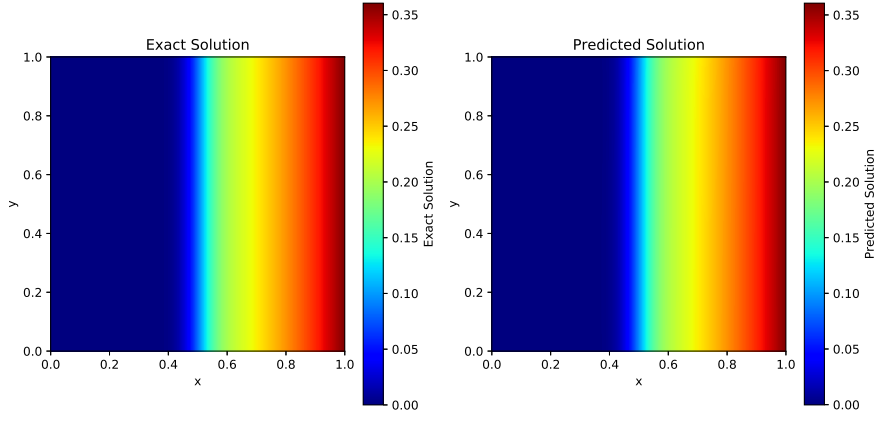


Figure 25: Radiation distribution with a Gaussian source, solved by PINN and exact at $k_e = 1m^{-1}$ for $x = y$.

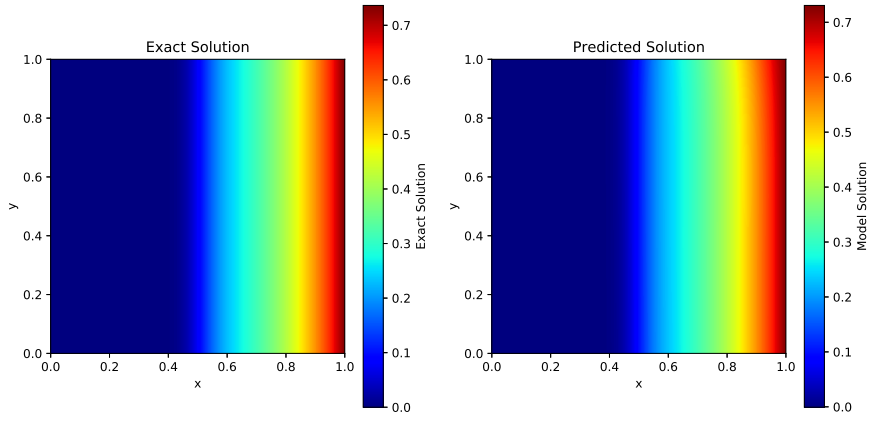


Figure 26: Radiation distribution with a Gaussian source, solved by PINN and exact at $k_e = 2m^{-1}$ for $x = y$.

Case	N_{int}	N_{sb}	$K - 1$	\bar{d}	λ	E_T	$\ I - I^*\ _{L^2}$	Training Time (sec.)
1	8192	4096	4	20	0.1	0.00029	0.0002	9
2	8192	4096	4	20	0.1	0.0008	0.0012	10
3	8192	4096	4	20	0.1	0.0002	0.003	17

Table 6: Results of the radiation transport equation for Gaussian-shaped emissive field along the diagonal.

3.2 Inverse problems

3.2.1 2D radiation distribution with Gaussian source term

The numerical experiment of section (3.1.4) is performed as an inverse problem using Algorithm 2.2. In this experiment, we excluded the boundary conditions. Figs.27 and 28 show the exact and predicted solutions of the RTE for $k_e = 0.1m^{-1}$ and $k_e = 1m^{-1}$, respectively. The errors, shown in Table 7, are minimal for different k_e values, demonstrating that the PINN is with high accuracy and at a meager computational cost. At $k_e = 1m^{-1}$, the relative average error of the mass-free method [50] is 0.7. At $k_e = 1m^{-1}$, the relative average error of the mass-free method(MSORTE form) [50] is 0.04. At $k_e = 1m^{-1}$, the relative error of the MRT lattice Boltzmann algorithm, as simulated by Feng et al. [15], is 2.5%. The PINN method demonstrates a relative error of 0.3% at $k_e = 1$, notably lower than that of other methods.

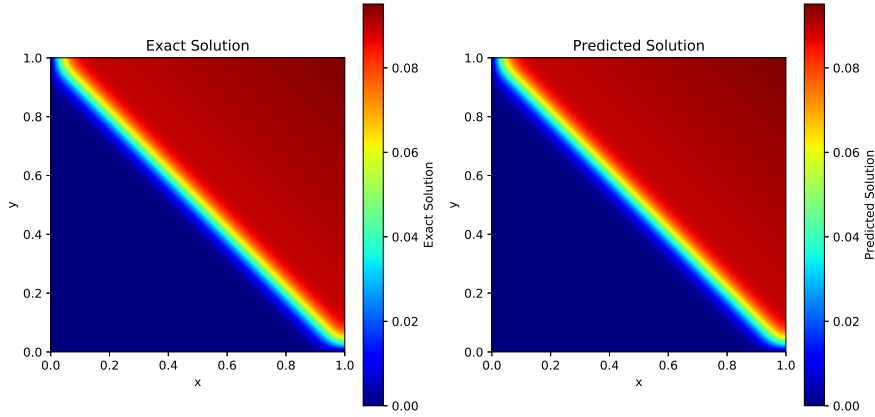


Figure 27: 2D Radiation distribution with a Gaussian source, solved by inverse PINN and exact at $k_e = 0.1m^{-1}$.

Case	N_{int}	N_d	$K - 1$	\bar{d}	λ	E_T	$\ I - I^*\ _{L^2}$	Training Time (sec.)
1	16384	8192	4	20	0.1	0.003	0.0008	36
2	16384	8192	4	20	0.1	0.003	0.0005	76

Table 7: Results for the 2D Radiation distribution with a Gaussian source(inverse).

4 Conclusion

Solving the RTE with graded index (2.1) presents a formidable challenge due to their inherent high-dimensional nature, especially when considering the most general scenario with high dimensions. Furthermore, incorporating diverse physical phenomena such as emission, absorption, and scattering, alongside the variability in optical parameters across the medium, adds complexity to devising efficient numerical algorithms. As highlighted earlier, existing methodologies often grapple with the curse of dimensionality, necessitating substantial computational resources to attain the desired level of precision. In our study, we propose an innovative solution to this challenge. Our approach, outlined in Algorithms 2.1 and 2.2, harnesses PINNs and sophisticated neural network architectures

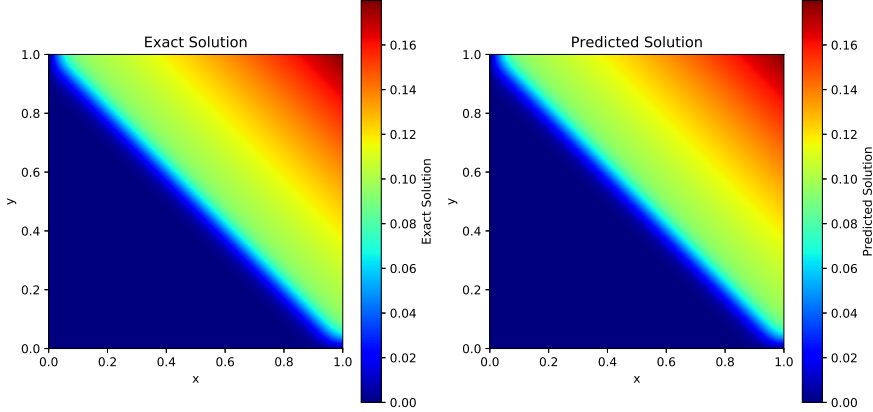


Figure 28: 2D Radiation distribution with a Gaussian source, solved by inverse PINN and exact at $k_e = 1m^{-1}$.

tailored specifically for approximating the radiative intensity outlined in the equation. Through iterative training using gradient descent, our network endeavors to minimize comprehensive loss function (2.15) and (2.16), respectively. This loss function encapsulates the residual error from integrating the neural network representation into the RTE (2.1). The residual errors are strategically positioned at training points, aligning with quadrature points based on a predefined quadrature rule. To alleviate the computational burden associated with high dimensionality, we employ Sobol low-discrepancy sequences as training points, optimizing efficiency while preserving accuracy.

Traditional numerical methods often encounter limitations when solving first-order equations, particularly in singular boundary conditions. To address these challenges, these methods typically convert the equations into second-order form to eliminate singularities at the boundaries before initiating the simulation. However, this reformulation can introduce inaccuracies, especially in scenarios with steep gradients or discontinuities. In their original first-order form, traditional methods are prone to numerical instabilities, often resulting in oscillations or wiggles in the solution. PINNs provide a robust alternative to overcome these challenges. PINNs embed the governing physics into the loss function by directly solving the first-order equations without requiring reformulation. This approach allows them to naturally handle boundary conditions and produce smooth, stable solutions, even in cases where traditional methods fail. Therefore, we posit that PINN algorithms 2.1 and 2.2 serve as a versatile, straightforward-to-implement, swift, and precise simulator for RTE phenomena. We demonstrate that this algorithm excels in speed and accuracy through numerical experiments. In essence, we contribute novel machine learning methodologies that offer a swift, user-friendly, and precise means of simulating various facets of radiation heat transfer in graded index phenomena. Our results showed that this approach worked well to reduce numerical errors, as there were no strange bumps in the results.

Declaration of competing interest

The authors declare that they have no competing interests.

Acknowledgment

The first author acknowledges the Ministry of Human Resource Development (MHRD), Government of India, for providing institutional funding and support at IIT Madras.

Appendix

An estimate of the generalization error for equation (2.1) is provided for the forward in Appendix D.1. An estimate of the generalization error for steady state equation (2.21) is provided for forward problems in Appendix D.2.

Appendix D.1. Assume $I \in L^2(\mathbf{D})$ is the unique weak solution to the RTE in graded-index media, where the coefficients $0 \leq k_e, k_s \in L^\infty(D)$, and phase function $\Phi(\mathbf{\Omega}, \mathbf{\Omega}') \in C^p(S \times S)$ for some $p > 0$. Let $I^* = I_\Theta \in C^p(\mathbf{D})$ be the solution generated by Algorithm 2.1 (forward PINN applied to the equation). Assume the condition $\max\{HK_V(I^*), HK_V(R_{int, \Theta^*})\} < \infty$, where HK_V represents the Hardy-Krause variation. Further, assume that Sobol points are used as training points $\xi_{int}, \xi_{sb}, \xi_{tb}$, and a Gauss-quadrature rule of order $a = a(p)$ is applied to approximate the scattering term in residual. Additionally, we assume that a refractive index $n = f(s) \in D$ are arbitrarily chosen in a manner consistent with the general model structure of the radiative transport equation. Under these assumptions:

$$n^2 k_a I_b(T_g) \leq n^2 k_a M I + f(s),$$

$$(\mathbf{\Omega} \cdot \nabla) I + \frac{1}{n \sin \theta} \frac{\partial}{\partial \varphi} ((s_1 \cdot \nabla n) I) + \frac{1}{n \sin \theta} \frac{\partial}{\partial \theta} (I(\mathbf{\Omega} \cos \theta - k) \cdot \nabla n) \leq n M I + (\mathbf{\Omega} \cdot \nabla_s) I, \quad M > 0.$$

The estimation of the generalized error for the forward problem is

$$(E_G)^2 \leq V \left((E_T^{tb})^2 + \nu (E_T^{sb})^2 + \nu (E_T^{int})^2 \right) + V V_2 \left(\frac{(\log(N_{tb}))^{2d}}{N_{tb}} + \nu \frac{(\log(N_{sb}))^{2d}}{N_{sb}} + \nu \frac{(\log(N_{int}))^{2d+1}}{N_{int}} + \nu N_S^{-2a} \right), \quad (4.1)$$

where:

$$\begin{aligned} \bar{V} &= (\|\mathbf{D}\|, \|\Phi\|_{C^p}, \|\hat{I}\|), \\ V &= \left(T + \nu V_1 \bar{T}^2 \exp(\nu V_1 T) \right), \\ V_1 &= \frac{2\nu(\|k_s\|_{L^\infty} + \|\Sigma_g\|_{L^\infty})}{4\pi}, \\ V_2 &= \max\{HK_V(R_{tb}^*)^2, HK_V(R_{sb}^*)^2, HK_V(R_{int}^*)^2, \bar{V}\}. \end{aligned}$$

Proof. We are following [29]

$$\mathcal{E}(I^*, \Phi) = \sum_{i=1}^{N_S} w_i^S \Phi(\mathbf{\Omega}, \mathbf{\Omega}_i^S) I^*(t, s, \mathbf{\Omega}_i^S) - \int_{4\pi} \Phi(\mathbf{\Omega}, \mathbf{\Omega}') I^*(t, s, \mathbf{\Omega}) d\Omega', \quad (4.2)$$

$$\bar{I} = I^* - I,$$

$$\begin{aligned} \frac{n}{c_0} \frac{\partial}{\partial t} \bar{I} + (k_e + \mathbf{\Omega} \cdot \nabla) \bar{I} + \frac{1}{n \sin \theta} \frac{\partial}{\partial \theta} \{ \bar{I}(\mathbf{\Omega} \cos \theta - k) \cdot \nabla n \} + \frac{1}{n \sin \theta} \frac{\partial}{\partial \varphi} \{ (s_1 \cdot \nabla n) \bar{I} \} \\ = n^2 k_a \bar{I}_b(T_g) + \frac{k_s}{4\pi} \int_{4\pi} \Phi(\mathbf{\Omega}, \mathbf{\Omega}') \bar{I}(t, s, \mathbf{\Omega}) d\Omega' + \mathcal{E}(I^*), \end{aligned} \quad (4.3)$$

We define

$$\begin{aligned} \bar{I}(0, s, \mathbf{\Omega}) &= R_{tb}^*, \quad (s, \mathbf{\Omega}) \in D \times S \\ \bar{I}(t, s, \mathbf{\Omega}) &= R_{sb}^*, \quad (t, s, \mathbf{\Omega}) \in \beta \end{aligned} \quad (A)$$

Multiplying Eq.(4.3) by \bar{I} on both side,

$$\begin{aligned} \frac{n}{2c_0} \frac{d\bar{I}^2}{dt} &= -k_e \bar{I}^2 - (\mathbf{\Omega} \cdot \nabla_s) \left(\frac{\bar{I}^2}{2} \right) - \frac{1}{n \sin \theta} \frac{\partial}{\partial \theta} \{ \bar{I}(\mathbf{\Omega} \cos \theta - k) \cdot \nabla n \} \bar{I} - \frac{1}{n \sin \theta} \frac{\partial}{\partial \varphi} \{ (s_1 \cdot \nabla n) \bar{I} \} \bar{I} \\ &\quad + n^2 k_a \bar{I}_b \bar{I}(T_g) - \frac{k_s}{4\pi} \int_{4\pi} \Phi(\mathbf{\Omega}, \mathbf{\Omega}') \bar{I}(t, s, \mathbf{\Omega}) \bar{I}((t, s, \mathbf{\Omega}')) d\Omega' + \mathcal{E}(I^*, \Phi) \bar{I}. \end{aligned} \quad (4.4)$$

We can observe that $(\mathbf{\Omega} \cdot \nabla) I + \frac{1}{n \sin \theta} \frac{\partial}{\partial \varphi} \{ (s_1 \cdot \nabla n) I \} + \frac{1}{n \sin \theta} \frac{\partial}{\partial \theta} \{ \bar{I}(\mathbf{\Omega} \cos \theta - k) \cdot \nabla n \} \leq M \bar{I} + (\mathbf{\Omega} \cdot \nabla_s) I$,
 $n^2 k_a \bar{I}_b(T_g) \leq n^2 k_a n M \bar{I} + f(s)$,

And

$$\int_{D \times S} |f(s) \bar{I}| ds d\mathbf{\Omega} \leq \int_{D \times S} |f|^2 ds d\mathbf{\Omega} + \int_{D \times S} |\bar{I}|^2 ds d\mathbf{\Omega}. \quad (4.5)$$

We substitute the values into Eq.(4.4), integrate the result over $D \times S$, and apply integration by part and Cauchy sequence and $k_e, k_s > 0$, and $t \in (0, T]$

$$\begin{aligned} \frac{n}{2c_0} \frac{d}{dt} \int_{D \times S} \bar{I}^2(t, s, \Omega) ds d\Omega &\leq \int_{D \times S} \bar{I}^2(t, s, \Omega) ds d\Omega - \int_{(\partial D \times S)_-} (\Omega \cdot k(s)) \frac{\bar{I}^2(t, s, \Omega)}{2} dk(s) d\Omega \\ &+ \int_{D \times S} \frac{k_s}{4\pi} \int_{4\pi} \Phi(\Omega, \Omega') \bar{I}(t, s, \Omega) \bar{I}(t, s, \Omega') d\Omega' d\Omega ds \\ &+ \int_{D \times S} |f|^2 ds d\Omega + \int_{D \times S} \frac{(\mathcal{E}(I^*, \Phi)(t, s, \Omega))^2}{2} d\Omega ds. \end{aligned} \quad (4.6)$$

In this case, $dk(s)$ signifies the surface measure on ∂D , and it can be defined as

$$\beta = (\partial D \times S)_- = \{(s, \Omega) \in \partial D \times S : \Omega \cdot k(s) \leq 0\},$$

And with $k(s)$ unit normal at $s \in \partial D$. Select a $\hat{T} \in (0, T]$ and integrate Eq.(4.6) over $(0, \bar{T})$,

$$\begin{aligned} \int_{D \times S} \bar{I}^2(\hat{T}, s, \Omega) ds d\Omega &\leq \int_{D \times S} \bar{I}^2(0, s, \Omega) dx d\Omega + 2\nu \int_0^{\hat{T}} \int_{D \times S} \bar{I}^2(t, s, \Omega) dt ds d\Omega \\ &+ \nu \int_{\beta} |\Omega \cdot k| \bar{I}^2(t, s, \Omega) dt dk(s) d\Omega + U + \int_{D \times S} |f|^2 d\Omega ds + \nu \int_D \frac{(\mathcal{E}(I^*, \Phi))^2}{2} dX. \end{aligned} \quad (4.7)$$

Let

$$U = 2\nu \int_0^{\bar{T}} \int_{D \times S} \frac{k_s}{4\pi} \int_{4\pi} \Phi(\Omega, \Omega') \bar{I}(t, s, \Omega) \bar{I}(t, s, \Omega') d\Omega d\Omega' ds dt. \quad (4.8)$$

The value of U in Eq.(4.7) can be determined through repeated application of the Cauchy-Schwartz inequality as follows:

$$\begin{aligned} U &\leq 2\nu \int_0^{\bar{T}} \int_{D \times S} \bar{I}^2(t, s, \Omega) d\Omega d\Omega' ds dt = \frac{2\nu(\|k_s\|_{L^\infty} + \|\Sigma_g\|_{L^\infty})}{4\pi} \int_0^{\bar{T}} \int_{D \times S} \bar{I}^2(t, s, \Omega) d\Omega d\Omega' ds dt \\ &= V_1 \int_0^{\bar{T}} \int_{D \times S} \bar{I}^2(t, s, \Omega) d\Omega d\Omega' ds dt. \end{aligned} \quad (4.9)$$

We get after identifying the constant from

$$\begin{aligned} \int_{D \times S} \bar{I}^2(t, s, \Omega) ds d\Omega &\leq \int_{D \times S} (R_{tb}^*)^2 ds d\Omega + \nu \int_{\beta} (R_{sb}^*)^2 dt dk(s) d\Omega \\ &+ c\|(R_{int}^*)\|_{L^2(D_T \times S)}^2 + \nu \int_D (\mathcal{E}(I^*, \Phi))^2 dX + \nu V_1 \int_0^{\bar{T}} \int_{D \times S} \bar{I}^2(t, s, \Omega) d\Omega d\Omega' ds dt, \end{aligned} \quad (4.10)$$

We apply the integral in Gronwall inequality form to Eq.(4.10) to obtain:

$$\begin{aligned} \int_{D \times S} \bar{I}^2(t, s, \Omega) ds d\Omega &\leq \left(1 + \nu V_1 \hat{T}^2 \exp^{\nu V_1 \hat{T}}\right) \\ &\times \left(\int_{D \times S} (R_{tb}^*)^2 ds d\Omega + \nu \int_{\beta} (R_{sb}^*)^2 dt dk(s) d\Omega \right) \\ &+ \left(1 + \nu V_1 \bar{T}^2 \exp^{\nu V_1 \bar{T}}\right) \\ &\times \left(\nu \|(R_{int}^*)\|_{L^2(D_T \times S)}^2 + (\mathcal{E}(I^*, \Phi))^2 dX \right), \end{aligned} \quad (4.11)$$

Integrating Eq.(4.11) over $(0, T)$

$$(E_G)^2 = \int_{\mathbf{D}} \tilde{I}^2(t, s, \mathbf{\Omega}) ds d\mathbf{\Omega} \leq \left(T + \nu V_1 \hat{T}^2 \exp^{\nu V_1 T} \right) \left(\int_{D \times S} (R_{tb}^*)^2 ds d\mathbf{\Omega} + \nu \int_{\beta} (R_{sb}^*)^2 dt dk(s) d\mathbf{\Omega} \right) \\ + \left(\hat{T} + \nu V_1 \hat{T}^2 \exp^{\nu V_1 \hat{T}} \right) \left(\nu \|R_{int}^*\|_{L^2(D_T \times S)}^2 + \mathcal{E}(I^*, \Phi)^2 dX \right). \quad (4.12)$$

The points used for training in ζ are Sobol quadrature points, therefore the training error E_T represents the quasi-Monte Carlo quadrature of the integral Eq.(4.12). Consequently, this aligns with the Koksma-Hlawaka inequality [6],

$$\int_{D \times S} (R_{tb}^*)^2 ds d\mathbf{\Omega} \leq (E_T^{tb})^2 + HK_V(R_{tb}^*)^2) \frac{(\log(N_{tb}))^{2d}}{N_{tb}}, \quad (4.13)$$

Similarly

$$\int_{\beta} (R_{sb}^*)^2 dt dk(s) d\mathbf{\Omega} \leq (E_T^{sb})^2 + HK_V(R_{sb}^*)^2) \frac{(\log(N_{sb}))^{2d}}{N_{sb}}, \quad (4.14)$$

$$c \|R_{int}^*\|_{L^2(D_T \times S)}^2 \leq (E_T^{int})^2 + HK_V(R_{int}^*)^2) \frac{(\log(N_{int}))^{2d+1}}{N_{int}}, \quad (4.15)$$

In this context, (Ω^S) for $1 \leq i \leq N_S$ represent points and weights of the Gauss quadrature rule $a = a(p)$ as

$$\int_{\mathbf{D}} (\mathcal{E}(I^*, \Phi))^2 dX \leq \bar{V} N_S^{-2a} \quad (4.16)$$

where $\bar{V} = (\|\mathbf{D}\|, \|\Phi\|_{C^p}, \|\hat{I}\|)$.

□

Appendix D.2. Let $I \in L^2(D \times S)$. Consider that I is a unique weak solution of the RTE Eq.(2.21) with coefficients $k_e, k_s \in L^\infty(D)$, where $0 \leq k_e, k_s$, and the bounds $\min(k_e), \max(k_e)$ and $\min(k_s), \max(k_s)$ correspond to the lower and upper limits of these coefficients. The phase function $\Phi(\mathbf{\Omega}, \mathbf{\Omega}')$ is assumed to lie in the space $C^p(S \times S)$ for some $p > 0$. Let $I^* = I_\Theta \in C^p(D \times S)$ represent the output of Algorithm 2.1, which addresses the forward problem for the RTE with a graded index medium. Suppose that both the Hardy-Krause variation $V_{HK}(I^*)$ and $V_{HK}(R_{int, \Theta^*})$ are finite, and that Sobol points ζ_{int}, ζ_{sb} are used as training points as previously defined. Furthermore, assume that a Gauss-quadrature rule of order $a = a(p)$ is applied to approximate the scattering term in residual. Now, assume $M > 0$, refractive index $n = f(s) \in D$ and that the following inequalities hold:

$$n^2 k_a I_b(T_g) \leq n^2 k_a M I + f(s),$$

and

$$(\mathbf{\Omega} \cdot \nabla) I + \frac{1}{n \sin \theta} \frac{\partial}{\partial \varphi} ((s_1 \cdot \nabla n) I) + \frac{1}{n \sin \theta} \frac{\partial}{\partial \theta} (I(\mathbf{\Omega} \cos \theta - k) \cdot \nabla n) \leq n M I + (\mathbf{\Omega} \cdot \nabla_s) I, \quad M > 0.$$

Under the assumption $l > 0$:

$$\left(\min(k_e) + \min(M) - \min(k_s) - 1 \right) - \frac{2\nu(\max(k_s) + \|\Sigma_g\|_{L^\infty})}{4\pi} > l, \quad (4.17)$$

In the above inequalities for $M > 0$, the generalization error for forward problems is estimated by:

$$(E_{G_{steady_f}})^2 \leq V \left(\nu (E_T^{sb})^2 + \nu (E_T^{int})^2 \right) \\ + V \left(\frac{(\log(N_{sb}))^{2d}}{N_{sb}} + \nu \frac{(\log(N_{int}))^{2d}}{N_{int}} + \nu N_S^{-2a} \right), \quad (4.18)$$

Where $\bar{V} = (\|\mathbf{D}\|, \|\Phi\|_{C^p}, \|\hat{I}\|)$, C^ε is a constant dependent on l And

$$V = \max \left(\frac{2}{l}, \frac{2}{l} V_{HK} (R_{sb}^*)^2, \frac{2C^\varepsilon}{l} (R_{int}^*)^2, \frac{2C^\varepsilon}{l} \bar{V} N_S^{-2a} \right).$$

Proof. We are following [29]

$$\mathcal{E}_{S_f}(I^*, \Phi) = \sum_{i=1}^{N_S} w_i^S \Phi(\mathbf{\Omega}, \mathbf{\Omega}_i^S) I^*(s, \mathbf{\Omega}_i^S) - \int_{4\pi} \Phi(\mathbf{\Omega}, \mathbf{\Omega}') I^*(s, \mathbf{\Omega}) d\mathbf{\Omega}', \quad (4.19)$$

$$\bar{I} = I^* - I,$$

$$\begin{aligned} (k_e + \mathbf{\Omega} \cdot \nabla) \bar{I} + \frac{1}{n \sin \theta} \frac{\partial}{\partial \theta} \{ \bar{I}(\mathbf{\Omega} \cos \theta - k) \cdot \nabla n \} + \frac{1}{n \sin \theta} \frac{\partial}{\partial \varphi} \{ (s_1 \cdot \nabla n) \bar{I} \} \\ = n^2 k_a \bar{I}_b(T_g) + \frac{k_s}{4\pi} \int_{4\pi} \Phi(\mathbf{\Omega}, \mathbf{\Omega}') \bar{I}(s, \mathbf{\Omega}) d\mathbf{\Omega}' + \mathcal{E}_{S_f}(I^*, \Phi), \end{aligned} \quad (4.20)$$

$$\bar{I}(t, s, \mathbf{\Omega}) = \mathbf{R}_{sb}^*, \quad (t, s, \mathbf{\Omega}) \in \beta_o, \quad (\text{A})$$

Multiplying Eq.(4.20) by \bar{I} on both side.

$$\begin{aligned} k_e \bar{I}^2 + \frac{1}{n \sin \theta} \frac{\partial}{\partial \theta} \{ \bar{I}(\mathbf{\Omega} \cos \theta - k) \cdot \nabla n \} \bar{I} - \frac{1}{n \sin \theta} \frac{\partial}{\partial \varphi} \{ (s_1 \cdot \nabla n) \bar{I} \} \bar{I} \\ = -(\mathbf{\Omega} \cdot \nabla_s) \left(\frac{\bar{I}^2}{2} \right) + n^2 k_a \bar{I}_b(T_g) \bar{I} + \frac{k_s}{4\pi} \int_{4\pi} \Phi(\mathbf{\Omega}, \mathbf{\Omega}') \bar{I}(s, \mathbf{\Omega}) \bar{I}(s, \mathbf{\Omega}') d\mathbf{\Omega}' + \mathcal{E}_{S_f}(I^*, \Phi) \bar{I}, \end{aligned} \quad (4.21)$$

We can observe that $\frac{1}{n \sin \theta} \frac{\partial}{\partial \varphi} \{ (s_1 \cdot \nabla n) \bar{I} \} + \frac{1}{n \sin \theta} \frac{\partial}{\partial \theta} \{ \bar{I}(\mathbf{\Omega} \cos \theta - k) \cdot \nabla n \} \leq M \bar{I}$, and $n^2 k_a \bar{I}_b(T_g) \leq n^2 k_a M \bar{I} + f(s)$.

Integrating over $D \times S$ and using Cauchy inequality for $k_e, k_s > 0$,

$$\begin{aligned} \int_{D \times S} \bar{I}^2(s, \mathbf{\Omega}) ds d\mathbf{\Omega} \leq - \int_{(\partial D \times S)_-} (\mathbf{\Omega} \cdot k(x)) \frac{\bar{I}^2(s, \mathbf{\Omega})}{2} dk(s) d\mathbf{\Omega} \\ + \int_{D \times S} \frac{k_s}{4\pi} \int_{4\pi} \Phi(\mathbf{\Omega}, \mathbf{\Omega}') \bar{I}(s, \mathbf{\Omega}) \bar{I}(s, \mathbf{\Omega}') d\mathbf{\Omega}' d\mathbf{\Omega} ds \\ + \int_{D \times S} f(s) \bar{I}(s, \mathbf{\Omega}) d\mathbf{\Omega} ds \\ + \int_{D \times S} (\mathcal{E}_{S_f}(I^*, \Phi) \bar{I}(s, \mathbf{\Omega})) d\mathbf{\Omega} ds, \end{aligned} \quad (4.22)$$

In this case, $dk(s)$ signifies the surface measure on ∂D , and it can defined as

$$\beta_o = (\partial D \times S)_- = \{ (s, \mathbf{\Omega}) \in \partial D \times S : \mathbf{\Omega} \cdot k(s) \leq 0 \}$$

and with $k(s)$ unit normal at $s \in \partial D$,

Let

$$U = 2\nu \int_{D \times S} \frac{k_s}{4\pi} \int_{4\pi} \Phi(\mathbf{\Omega}, \mathbf{\Omega}') \bar{I}(s, \mathbf{\Omega}) \bar{I}(s, \mathbf{\Omega}') d\mathbf{\Omega}' d\mathbf{\Omega} ds, \quad (4.23)$$

Now U in Eq.(4.22) can be estimated by successive application of Cauchy-Schwartz inequality as

$$\begin{aligned} U \leq 2\nu \int_{D \times S} \bar{I}^2(s, \mathbf{\Omega}) d\mathbf{\Omega} d\mathbf{\Omega}' ds = \frac{2\nu(\|k_s\|_{L^\infty} + \|\Sigma_g\|_{L^\infty})}{4\pi} \int_{D \times S} \bar{I}^2(s, \mathbf{\Omega}) d\mathbf{\Omega} d\mathbf{\Omega}' ds \\ = V_1 \int_{D \times S} \bar{I}^2(s, \mathbf{\Omega}) d\mathbf{\Omega} d\mathbf{\Omega}' ds, \end{aligned} \quad (4.24)$$

Utilizing integration by parts, and applying the presumed limits on k_e , k_s , and M , we derive:

$$\begin{aligned} \left(\min(k_e) + \min(M) - \min(k_s) - 1 \right) \int_{D \times S} \bar{I}^2(s, \Omega) ds d\Omega &\leq \nu \int_{\beta_o} (R_{sb}^*)^2 dk(s) d\Omega \\ &+ \int_{D \times S} (R_{int}^*) \bar{I} d\Omega ds + \nu \int_{D \times S} (\mathcal{E}_{S_f}(I^*, \Phi)) \bar{I} dX \quad (4.25) \\ &+ \nu V_1 \int_{D \times S} \bar{I}^2(s, \Omega) d\Omega d\Omega' ds, \end{aligned}$$

Given assumption 4.17, \exists an $\varepsilon > 0$ such that

$$\left(\min(k_e) + \min(M) - \min(k_s) - 1 \right) - \frac{2\nu(\max(k_s) + \|\Sigma_g\|_{L^\infty})}{4\pi} - 2\varepsilon > \frac{l}{2},$$

We apply the ε -version of Cauchy's inequality.

$$\int_{D \times S} \bar{I}^2(s, \Omega) ds d\Omega \leq \frac{2}{l} \int_{\beta_o} (R_{sb}^*)^2 dk(s) d\Omega + \frac{2C^\varepsilon}{l} \int_{D \times S} (R_{int}^*)^2 d\Omega + \mathcal{E}_{S_f}(I^*, \Phi)^2 dX. \quad (4.26)$$

□

References

- [1] A. I. Arbab. On compton scattering in dielectric medium. *Optik*, 127(20):8536–8541, 2016.
- [2] G. Bai, U. Koley, S. Mishra, and R. Molinaro. Physics informed neural networks (pinns) for approximating nonlinear dispersive pdes. *J. Comp. Math.*, 39:816–847, 2021.
- [3] D. Baillis, R. Coquard, J. H. Randrianalisoa, L. A. Dombrovsky, and R. Viskanta. Thermal radiation properties of highly porous cellular foams. *Special Topics & Reviews in Porous Media: An International Journal*, 4(2), 2013.
- [4] A. R. Barron. Universal approximation bounds for superpositions of a sigmoidal function. *IEEE Transactions on Information theory*, 39(3):930–945, 1993.
- [5] C. Beck, S. Becker, P. Grohs, N. Jaafari, and A. Jentzen. Solving the kolmogorov pde by means of deep learning. *Journal of Scientific Computing*, 88:1–28, 2021.
- [6] R. E. Caflisch. Monte carlo and quasi-monte carlo methods. *Acta numerica*, 7:1–49, 1998.
- [7] G. Cybenko. Approximations by superpositions of a sigmoidal function. *Mathematics of Control, Signals and Systems*, 2:183–192, 1989.
- [8] T. De Ryck, A. D. Jagtap, and S. Mishra. Error estimates for physics-informed neural networks approximating the navier–stokes equations. *IMA Journal of Numerical Analysis*, 44(1):83–119, 2024.
- [9] T. De Ryck and S. Mishra. Error analysis for physics-informed neural networks (pinns) approximating kolmogorov pdes. *Advances in Computational Mathematics*, 48(6):79, 2022.
- [10] T. De Ryck, S. Mishra, and R. Molinaro. wpinns: Weak physics informed neural networks for approximating entropy solutions of hyperbolic conservation laws. *SIAM Journal on Numerical Analysis*, 62(2):811–841, 2024.
- [11] V. Dolean, A. Heinlein, S. Mishra, and B. Moseley. Finite basis physics-informed neural networks as a schwarz domain decomposition method. In *International Conference on Domain Decomposition Methods*, pages 165–172. Springer, 2022.
- [12] H. Ebrahimi, A. Zamaniyan, J. S. S. Mohammadzadeh, and A. A. Khalili. Zonal modeling of radiative heat transfer in industrial furnaces using simplified model for exchange area calculation. *Applied Mathematical Modelling*, 37(16-17):8004–8015, 2013.
- [13] R. Evans, J. Jumper, J. Kirkpatrick, L. Sifre, T. Green, C. Qin, A. Zidek, A. Nelson, A. Bridgland, H. Penedones, et al. De novo structure prediction with deeplearning based scoring. *Annu Rev Biochem*, 77(363-382):6, 2018.
- [14] Y.-Y. Feng and C.-H. Wang. Discontinuous finite element method with a local numerical flux scheme for radiative transfer with strong inhomogeneity. *International Journal of Heat and Mass Transfer*, 126:783–795, 2018.

- [15] Y.-Y. Feng and C.-H. Wang. On the performance of a mrt lattice boltzmann algorithm for transient radiative transfer problems. *International Communications in Heat and Mass Transfer*, 128:105628, 2021.
- [16] A. Fokou, R. Tapimo, G. L. Ymeli, R. Tchinda, and H. T. T. Kamdem. Radiation distribution in inhomogeneous atmosphere-ocean system by discrete spherical harmonics method. *Journal of Quantitative Spectroscopy and Radiative Transfer*, 270:107707, 2021.
- [17] I. Goodfellow. *Deep learning*. MIT press, 2016.
- [18] K. Hornik, M. Stinchcombe, and H. White. Multilayer feedforward networks are universal approximators. *Neural networks*, 2(5):359–366, 1989.
- [19] Q. A. Huhn, M. E. Tano, and J. C. Ragusa. Physics-informed neural network with fourier features for radiation transport in heterogeneous media. *Nuclear Science and Engineering*, 197(9):2484–2497, 2023.
- [20] A. D. Jagtap and G. E. Karniadakis. Extended physics-informed neural networks (xpinns): A generalized space-time domain decomposition based deep learning framework for nonlinear partial differential equations. *Communications in Computational Physics*, 28(5), 2020.
- [21] A. D. Jagtap, E. Kharazmi, and G. E. Karniadakis. Conservative physics-informed neural networks on discrete domains for conservation laws: Applications to forward and inverse problems. *Computer Methods in Applied Mechanics and Engineering*, 365:113028, 2020.
- [22] I. E. Lagaris, A. Likas, and D. I. Fotiadis. Artificial neural networks for solving ordinary and partial differential equations. *IEEE transactions on neural networks*, 9(5):987–1000, 1998.
- [23] E. W. Larsen, F. Malvagi, and G. Pomraning. One-dimensional models for neutral particle transport in ducts. *Nuclear science and engineering*, 93(1):13–30, 1986.
- [24] L. Liu. Finite volume method for radiation heat transfer in graded index medium. *Journal of Thermophysics and Heat Transfer*, 20(1):59–66, 2006.
- [25] L. Liu. Meshless local petrov-galerkin method for solving radiative transfer equation. *Journal of thermophysics and heat transfer*, 20(1):150–154, 2006.
- [26] L. Liu. Least-squares finite element method for radiation heat transfer in graded index medium. *Journal of Quantitative Spectroscopy and Radiative Transfer*, 103(3):536–544, 2007.
- [27] X. Liu, Y. Huang, C.-H. Wang, and K. Zhu. Solving steady and transient radiative transfer problems with strong inhomogeneity via a lattice boltzmann method. *International Journal of Heat and Mass Transfer*, 155:119714, 2020.
- [28] L. Lu, X. Meng, Z. Mao, and G. E. Karniadakis. Deepxde: A deep learning library for solving differential equations. *SIAM review*, 63(1):208–228, 2021.
- [29] S. Mishra and R. Molinaro. Physics informed neural networks for simulating radiative transfer. *Journal of Quantitative Spectroscopy and Radiative Transfer*, 270:107705, 2021.
- [30] S. Mishra and R. Molinaro. Estimates on the generalization error of physics-informed neural networks for approximating a class of inverse problems for pdes. *IMA Journal of Numerical Analysis*, 42(2):981–1022, 2022.
- [31] S. Mishra and R. Molinaro. Estimates on the generalization error of physics-informed neural networks for approximating pdes. *IMA Journal of Numerical Analysis*, 43(1):1–43, 2023.
- [32] B. Moseley, A. Markham, and T. Nissen-Meyer. Finite basis physics-informed neural networks (fbpinns): a scalable domain decomposition approach for solving differential equations. *Advances in Computational Mathematics*, 49(4):62, 2023.
- [33] A. Paszke, S. Gross, S. Chintala, G. Chanan, E. Yang, Z. DeVito, Z. Lin, A. Desmaison, L. Antiga, and A. Lerer. Automatic differentiation in pytorch. *NIPS Autodiff Workshop*, 2017.
- [34] T. Pichard, G. W. Alldredge, S. Brull, B. Dubroca, and M. Frank. An approximation of the m 2 closure: application to radiotherapy dose simulation. *Journal of Scientific Computing*, 71(1):71–108, 2017.
- [35] M. Raissi, P. Perdikaris, and G. E. Karniadakis. Physics-informed neural networks: A deep learning framework for solving forward and inverse problems involving nonlinear partial differential equations. *Journal of Computational physics*, 378:686–707, 2019.
- [36] J. H. Randrianalisoa, L. A. Dombrovsky, W. Lipiński, and V. Timchenko. Effects of short-pulsed laser radiation on transient heating of superficial human tissues. *International Journal of Heat and Mass Transfer*, 78:488–497, 2014.

- [37] R. Riganti and L. D. Negro. Auxiliary physics-informed neural networks for forward, inverse, and coupled radiative transfer problems. *Applied Physics Letters*, 123(17), 2023.
- [38] M. Seaid, M. Frank, A. Klar, R. Pinnau, and G. Thömmes. Efficient numerical methods for radiation in gas turbines. *Journal of Computational and Applied Mathematics*, 170(1):217–239, 2004.
- [39] K. Shukla, A. D. Jagtap, and G. E. Karniadakis. Parallel physics-informed neural networks via domain decomposition. *Journal of Computational Physics*, 447:110683, 2021.
- [40] J. Stoer. R. bulirsch introduction to numerical analysis springer-verlag. *Texts in Applied Mathematics*, 12:30, 2002.
- [41] Y.-S. Sun and B.-W. Li. Chebyshev collocation spectral method for one-dimensional radiative heat transfer in graded index media. *International Journal of Thermal Sciences*, 48(4):691–698, 2009.
- [42] C.-A. Wang, H. Sadat, and V. Le Dez. Meshless method for solving multidimensional radiative transfer in graded index medium. *Applied Mathematical Modelling*, 36(11):5309–5319, 2012.
- [43] S. Wang, X. Yu, and P. Perdikaris. When and why pinns fail to train: A neural tangent kernel perspective. *Journal of Computational Physics*, 449:110768, 2022.
- [44] L.-Y. Wei, H. Qi, Z.-T. Niu, Y.-T. Ren, and L.-M. Ruan. Reverse monte carlo coupled with runge-kutta ray tracing method for radiative heat transfer in graded-index media. *Infrared Physics & Technology*, 99:5–13, 2019.
- [45] D. Yarotsky. Error bounds for approximations with deep relu networks. *Neural networks*, 94:103–114, 2017.
- [46] H.-L. Yi, F.-J. Yao, and H.-P. Tan. Lattice boltzmann model for a steady radiative transfer equation. *Physical Review E*, 94(2):023312, 2016.
- [47] G. L. Ymeli and C.-H. Wang. Generalized lattice boltzmann method for radiative transfer problem in slab and irregular graded-index media. *Physical Review E*, 107(1):015302, 2023.
- [48] J. Yu, L. Lu, X. Meng, and G. E. Karniadakis. Gradient-enhanced physics-informed neural networks for forward and inverse pde problems. *Computer Methods in Applied Mechanics and Engineering*, 393:114823, 2022.
- [49] J. Zhao, J. Tan, and L. Liu. A deficiency problem of the least squares finite element method for solving radiative transfer in strongly inhomogeneous media. *Journal of Quantitative Spectroscopy and Radiative Transfer*, 113(12):1488–1502, 2012.
- [50] J. Zhao, J. Tan, and L. Liu. A second order radiative transfer equation and its solution by meshless method with application to strongly inhomogeneous media. *Journal of Computational Physics*, 232(1):431–455, 2013.